O_2-Oxidation of Individual Graphite and Graphene Nanoparticles in the 1200 – 2200 K Range: Particle-to-Particle Variations and the Evolution of the Reaction Rates and Optical Properties

Daniel J. Rodriguez, Chris Y. Lau, Bryan A. Long, Susanna An Tang, Abigail M. Friese, and Scott L. Anderson[*]

Department of Chemistry, University of Utah, 315 S. 1400 E., Salt Lake City, UT 84112

[*]*Corresponding author: anderson@chem.utah.edu*

ABSTRACT: The kinetics for O_2 oxidation of individual graphite and graphene platelet nanoparticles (NPs) were studied as a function of temperature (1200 to 2200 K) at varying oxygen partial pressures, using a single nanoparticle mass spectrometry method. NP temperature (T_{NP}) was measured by measuring the NP thermal emission spectra during the kinetics studies. The initial oxidation efficiency is found to peak in the 1200 to 1500 K range, dropping by an order of magnitude as T_{NP} was increased above 2000 K. There were large NP-to-NP variations in the oxidation rates, attributed to variations in the NP surface structure. In addition, the oxidation efficiencies decreased, non-monotonically, as the NPs reacted, by factors of between 10 and 300. This evolution of reactivity is attributed to changes in the NP surface structure due to the combination of oxidation and annealing. The optical properties, including wavelength dependence of the emissivity, and the absorption cross section for the 532 nm heating laser, also tend to evolve as the NPs oxidize, but differently for each individual NP, presumably reflecting differences in the initial structures, and how they evolve under different reaction conditions.

KEYWORDS: graphite, graphene, nanoparticle, oxidation, oxygen, single, evolution

The surface chemistry of nanoparticles (NPs) is important in many application areas, but most measurements of nano-surface chemistry are averaged over broad distributions of size, shape, and nanostructure. We recently demonstrated an approach to measuring quantitative reaction kinetics for individual NPs, with NP temperature (T_{NP}) determined from the single NP emission spectrum.[1-2] A study of the sublimation kinetics for graphite and graphene NPs was recently reported, showing Arrhenius kinetics with large variations in area-normalized rates and activation energies from one NP to the next.[3] The rates and activation energies gradually evolved as the NPs sublimed, attributed to changes in the NP surface structures, and these changes were also shown to be correlated with the emission brightness of the NPs. Here we report an initial study of a more complex process – O_2 oxidative etching of graphite and graphene NPs. Complex behavior is observed, including substantial NP-to-NP variations in rates, evolution of rates over time that is non-monotonic or oscillatory, and in some experiments, final states that are nearly inert to oxidation. These changes in oxidation rates are accompanied by substantial changes in the NP optical properties.

High temperature oxidation of various carbon materials has been studied extensively due to its importance in combustion of coal and chars, and because carbon is used in high temperature materials and thermal protection layers in applications where reactions with air determine stability. Many experimental[4-14] and theoretical[15-29] studies have focused on graphite or graphene, because these materials are important, and also have well understood structure and properties, making them useful model systems for more complex carbon materials. Most experiments on graphite oxidation kinetics or dynamics have concentrated on temperatures below ~2000 K, where the oxidation rates are highest. The rates depend strongly on the structure of the graphite surface, as well as the temperature. Perfect, fully-sp^2-coordinated basal plane sites are essentially inert,[5-6] and oxidation

studies of basal surfaces have typically used sputtering or other methods to create defects, where under-coordinated or strained sites are present. STM studies have shown that reaction at basal plane defects tends to etch laterally, creating etch pits or channels in the top basal plane, rather than attacking the underlying perfect basal plane.[10-11, 13, 30-31] Under-coordinated sites are also exposed at the perimeter of graphitic basal planes, and these edge sites are substantially more reactive than basal plane sites, with reactivity persisting to higher temperatures.[4]

Graphitic carbon oxidation by O_2 at temperatures above ~1200 K can be thought of as requiring O_2 dissociative adsorption on the surface, forming transient oxygenated surface complexes, followed by decomposition of the complexes to release gaseous products. The dissociative adsorption probability depends on the energetics of the various surface oxygen complexes (carbonyls, semiquinones, epoxides, …).[9, 15, 17-19, 21-25, 32-53] which depend on the local structure at the O_2 collision site. Once surface oxygen complexes form, they may decompose by CO or CO_2 desorption, but molecular beam studies have revealed that desorption of O_2 and O, the latter particularly at high temperatures, are also important, causing the etching rate to drop.[14] Further complicating the mechanism is the theoretical finding that the stability of surface oxygen complexes, and the activation energies for loss of CO or CO_2 from them, are strongly affected by the presence of nearby adsorbed oxygen. For example, the CO desorption energy from a semiquinone site was calculated to be ~335 kJ/mol,[17, 21, 47, 54] dropping by more than 100 kJ/mol if there was an adjacent epoxy group.[54] Similarly, the CO desorption energies for surface carbonyls were estimated to drop by between ~20% and 80% in the presence of different neighboring oxygenated groups.[15] The interplay between these factors, and the evolution of the NP surface site distributions over time, are expected to result in a complex dependence of the oxidation rates on P_{O2}, T_{NP}, and time.

We report kinetics measured by several different protocols, designed to probe different aspects of the oxidation mechanism. These include stepped heat ramps at constant oxygen pressure (P_{O2}), stepped P_{O2} ramps at constant T_{NP}, and oxidation at constant T_{NP} and P_{O2}. The results are discussed in terms of the expected atomic scale structure of the NPs, and the structural evolution that occurs due to a combination of site-specific etching, and annealing.

Results

As shown below, the oxidation kinetics of individual graphitic NPs can depend in complicated ways on T_{NP}, the O_2 partial pressure (P_{O2}), and on reaction time. In the following, we use three different protocols to probe different aspects of the NP oxidation behavior, including experiments at constant P_{O2} with variable T_{NP}, at constant T_{NP} with variable P_{O2}, and with both T_{NP} and P_{O2} held constant. A few examples of each protocol are presented here; additional examples are reported in the **Supporting Information**.

Variable T_{NP} - constant P_{O2} experiments

For an NP trapped in an O_2-containing atmosphere at high T_{NP}, changes in mass vs. time may result from oxidation (CO, CO_2 elimination), sublimation, or from reactions of the NP with background gasses in the vacuum chamber. Therefore, experiments of the type shown in **Fig. 1A** were done to allow the oxidation rate to be corrected for the effects of sublimation and/or background reactions. In this example, a single graphene platelet NP of initial mass ~75.0 MDa was trapped, and held at 1200 K for charge stepping, as shown in **Fig. S1**, which also shows the raw F_z measurements, omitted from **Fig. 1** for clarity. For reference, note that a graphene platelet with this mass, and 5 nm thickness (the average for the graphene feedstock), would have lateral dimensions of ~105 nm, but a spherical NP with the bulk graphite density would have ~47.2 nm diameter. At the beginning of the record shown in **Fig. 1**, T_{NP} (red circles) was set to 1200 K, and

then ramped in 100 K steps to 1500 K, holding each T_{NP} value for ~30 minutes. During the initial and final ~10 minutes of each constant T_{NP} period (unshaded background), only UHP argon at 2.0 mTorr was added to the trap, thus allowing measurement of the baseline rate of mass loss, due to the combination of sublimation and reactions with background gases. Mass measurements are shown as open circles, and linear fits to M vs. time used to extract the mass loss rates are shown as superimposed lines. For the middle ~10 minutes at each T_{NP}, O_2 was added to the trap atmosphere at a partial pressure (P_{O2}) of 4.3 x 10^{-5} Torr (shaded background), allowing the mass loss from the combination of oxidation + baseline processes to be measured. The stepwise heat ramp was repeated for a total of three times, over the course of ~9.5 hours, to allow the effects of NP structural evolution to be observed as the NP mass dropped to less than 1/3rd of the initial mass. In addition to the mass and T_{NP}, the figure shows the emission intensity (I_{NP}), integrated from 600 to 1600 nm, measured in concert with each mass point.

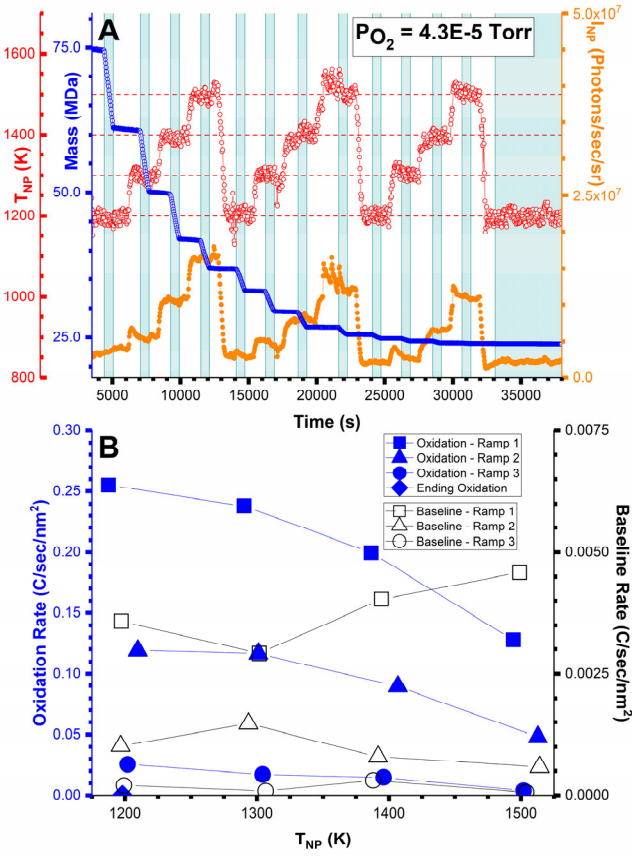

Figure 1: A). Raw sublimation and oxidation data for a 75.0 MDa graphene NP in the 1200 K to 1500 K. B). Oxidation and baseline rates are plotted for the three T_{NP} ramps.

Several points are obvious from the raw data. In this relatively low T_{NP} range, oxidation is much faster than the baseline mass loss rate, as shown by the large increase in the slope of M vs. time when O_2 was added to the trap. It is also clear that over the course of the experiment, the NP became substantially less reactive, *i.e.*, the mass loss rates at each T_{NP} were much slower in the final heat ramp, compared to the first. The decrease in reactivity is also obvious in the total mass losses in the 1st, 2nd, and 3rd heat ramps, which were ~51%, ~32%, and ~4% of the NP mass *at the start of each heat ramp*. All things being equal, the rates of surface reactions should be proportional to the surface area, which would scale like $M^{2/3}$, assuming that the NP shape remains roughly constant. Thus at the end of the experiment, when the mass was 1/3rd the initial mass, this surface area factor was $\sim 0.33^{2/3} \approx 47\%$, the rate should have slowed by half due to surface area loss. Instead, the rate slowed by roughly an order of magnitude, indicating that factors other than surface area are important. Examples of even more dramatic rate slowing are presented and discussed below.

The integrated emission intensities, I_{NP}, measured at each T_{NP} dropped by ~1/3rd over the course of the experiment. Macroscopic blackbody emission scales like the emitting surface area, but for NPs much smaller than the wavelength (λ), the emissivity scales like radius/λ.[60] Therefore, emission intensity might be expected to scale like the NP volume, *i.e.*, like M. In **Fig. 1**, the emission intensity dropped by ~1/3rd as the mass dropped by ~2/3rd, *i.e.*, the final intensity was about twice what might have been expected from the change in NP mass. In fact, we often have observed significant deviations from this expectation for carbon NPs,[1, 3] with emission brightness sometimes actually increasing as NPs shrink, but also sometimes decreasing faster than the mass.

Fig. 1B shows the rates vs. T_{NP} for the baseline processes (sublimation+background reactions – "R_{base}", open black symbols) and for oxidation ("R_{oxid}", solid blue symbols) extracted

from the slopes in **Fig. 1A**. The R_{base} values are simply the mass loss rates measured when only Ar was added to the trap, averaging the rates measured before and after each oxidation period. Several observations indicate that for the low T_{NP} range studied in this experiment, sublimation is a minor contributor to the baseline rate. Note that R_{base} was nearly T_{NP} independent – unlikely for an endothermic process like sublimation. Indeed, we previously studied graphite and graphene NP sublimation in the 1800 K to 2100 K range,[3] and if the Arrhenius rate law expressions from those experiments are used to estimate the sublimation rate in the 1200 K to 1500 K range, the conclusion is that sublimation contributes less than a few percent of the R_{base} values shown in **Fig. 1B**. Thus for this low T_{NP} regime, R_{base} is attributed mostly to reactions with contaminants present in the chamber background at partial pressures in the 10^{-7} Torr range. The most likely contributor is O_2, which we expect in the background because the experiments involved repeated O_2 exposures.

The R_{oxid} values shown in **Fig. 1B** were determined from the mass loss rates measured when O_2 was added to the trap, by subtracting the R_{base} values measured as described above. Thus, the R_{oxid} values are corrected for whatever process contributed to R_{base} for each T_{NP} point. Over the T_{NP} range of this experiment, the oxidation rates are fast compared to R_{base} (note 40x scale difference), as was clear from the raw data. To approximately correct for the expected decrease in rates due to decreasing surface area of the shrinking NP, and to allow comparison of rates for NPs of different sizes, both R_{base} and R_{oxid} have been put on a surface-area-normalized basis (C atoms lost/second/nm^2 of NP surface area), by dividing the raw rates from **Fig. 1A** (C atoms lost/second) by the NP surface area estimated from the NP mass, averaged over each time interval used in rate determinations. Because we don't know the NP shapes, the surface areas were estimated assuming spherical shape with the bulk graphite density.[61] This approximation gives

lower limits for the surface areas, hence upper limits for the area-normalized rates – more realistic estimates of NP structure and surface area are discussed below. Note also that our experiment provides no information about the gaseous products, but other researchers have measured the CO/CO_2 branching ratio, which is dominated by CO, particularly at high temperatures.[4-5, 14, 33, 62-63] In addition, Minton and co-workers have observed significant branching for desorption of O atoms from carbon undergoing oxidation at high temperatures,[14] which is a competing process that would not be detectable in our experiments.

In the low T_{NP} range explored in **Fig. 1**, the R_{oxid} values were weakly temperature dependent, decreasing slowly with increasing T_{NP} in all three heat ramps. This behavior is generally consistent with measurements of bulk graphite oxidation, where rates typically were found to peak at intermediate temperatures, falling off at high temperatures.[4-5, 64] The peak temperatures and rates in those experiments varied significantly with the nature of the graphitic surface studied, as well as the reaction conditions. We can roughly estimate the net efficiency of the O_2 collisions by comparing the number of C atoms lost/sec/nm^2 of surface area, to the rate of O_2 collision *per* nm^2, calculated from the O_2 partial pressure. The mean free path for the Ar and O_2 in these experiments (~0.05 m) is a factor of ~10 larger than the inner radius of the trap electrodes, thus we can assume that the gas temperature is essentially that of the trap electrodes, ~300 K. In that case, for 4.3 x 10^{-5} Torr of O_2, there would be ~150 O_2 collisions/sec/nm^2 of surface area, and even the maximum value of R_{oxid} (0.25 C/sec/nm^2) corresponds to well below one percent probability for removing a carbon atom *per* O_2 collision.

Perhaps the most interesting observation is that R_{oxid} decreased by an order of magnitude over the course of the experiment. As already noted, the area-normalized rates plotted in **Fig. 1B** are approximately corrected for the decrease in NP surface area as the NP was oxidized, thus we

conclude that the inherent reactivity of the NP surface toward O_2 decreased substantially as the NP was heated and exposed to Ar and O_2. Reaction of O_2 with hot graphitic surfaces has been studied extensively both experimentally[4-11, 13, 31, 58, 64-66] and theoretically.[16, 18, 20, 24-26, 28-29, 48, 54, 67] It has been shown that perfect basal plane sites, where all the C atoms are fully coordinated, are quite inert. For example, Barber *et al.*[6] estimated that the sticking coefficient at 673 K for O_2 on basal plane sites was ~10^{-14}, increasing by seven orders of magnitude if the graphite was sputtered to create defects. Thus, for the low T_{NP} values in **Fig. 1**, we expect that oxidation should be dominated by reactions at under-coordinated sites at basal plane defects or edges. The relatively high initial reactivity suggests that this NP had an initial structure with a relatively large number of such sites, and the decrease in reactivity is attributed to evolution of the NP surface site distribution toward greater average stability. Such evolution is not unexpected because oxidation will tend to preferentially occur at the reactive sites, and thus will tend to etch away asperities or other regions of the NP that have large numbers of such sites. At the low temperatures in this experiment, sublimation would have a relatively small effect on the NP surface, but various annealing processes may also alter the NP surface structure.

Two similar examples of single graphene platelet NP oxidation are shown in **Figs. S3** and **S4**. In the first, a graphene NP of ~45.0 MDa initial mass was subjected to a single stepwise heat ramp from 1200 K to 1700 K (the NP was lost before a second ramp could be done). The behavior was qualitatively similar to that for the graphene NP in **Fig. 1**, with R_{oxid} substantially faster than R_{base} at all temperatures. For this NP, R_{oxid} *increased* slowly from 1200 K to 1550 K, reaching a maximum value of 0.05 C/sec/nm^2, then fell to about half that value by 1700 K. The graphene NP in **Fig. S4** had initial mass of ~37.6 MDa, and was subjected to stepwise heating from 1200 K to 2000 K, with part of a 2nd heat ramp completed before the NP was lost. The behavior at low

temperatures was similar to that of the other two graphene NPs, and R_{oxid} was found to peak broadly in the 1300 – 1500 K range with a maximum value of ~0.05 C/sec/nm^2, falling at higher T_{NP}. One significant difference was that for $T_{NP} \geq 1800$ K, the sublimation increased rapidly with T_{NP}, dominating the mass loss at 2000 K. The three graphene NPs had broadly similar oxidation behavior at low T_{NP}, with R_{oxid} falling at high T_{NP}, however, the maximum area-normalized rates varied by a factor of ~five for the different NPs. Such large NP-to-NP variations are not surprising, and have also been seen in the sublimation rates of graphitic NPs.[3] We attribute the variability to structural heterogeneity of the graphene NPs, where each has different distributions of the under-coordinated sites that make the dominant contributions to the oxidation activity.

The next examples are for graphite NPs. **Fig. 2** summarizes a two-ramp experiment for a graphite NP that also

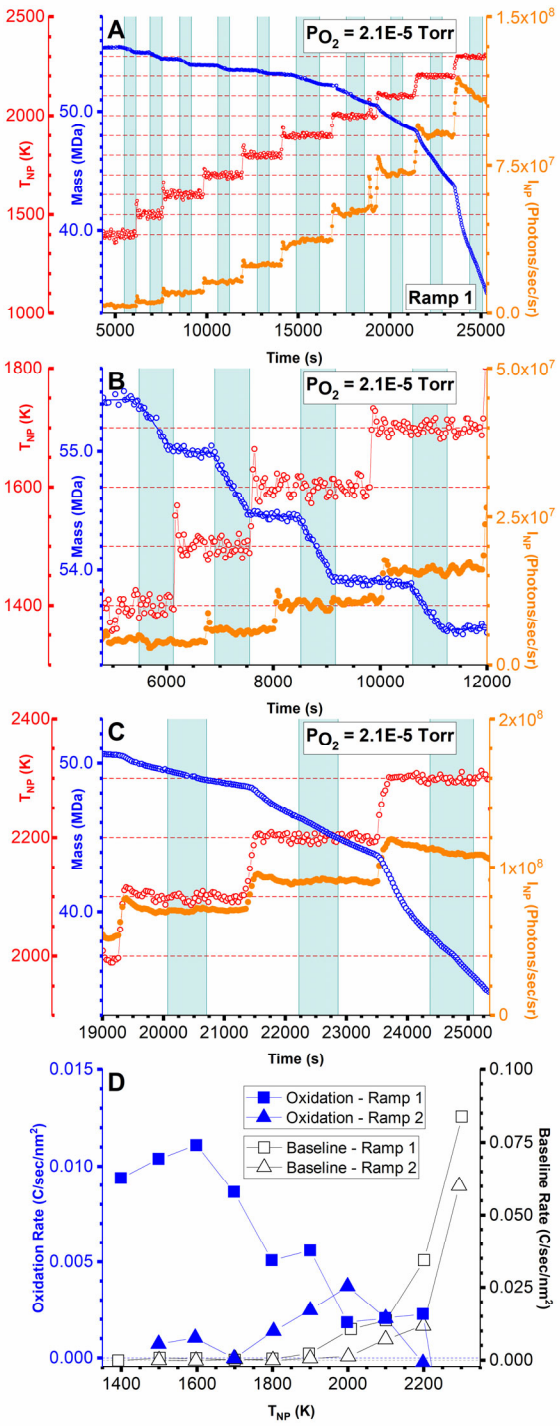

Figure 2: A). Sublimation and oxidation for a 55.5 MDa graphite NP at P_{O2} = 2.1 x 10^{-5} Torr. B). Expanded view for 1400 K to 1700 K. C). Expanded view for 2100 K to 2300 K. D). R_{oxid} and R_{base} versus T_{NP} for 1st and 2nd T_{NP}

extended into a higher T_{NP} range. A 55.5 MDa graphite NP was trapped and charge stepped at T_{NP} ≤ 1300 K prior to the start of the data record shown. This NP was subjected to two heat ramps from 1400 K to 2300 K in 100 K steps, each step lasting ~30 minutes. The first of these heat ramps is shown in **Fig. 2A-C** and the second is shown in **Fig. S5**. As in **Fig. 1**, mass vs. time was measured at the beginning and end of each step with just argon added to the trap, to determine the baseline mass loss rate, and 2.1 x 10^{-5} Torr of O_2 was added for the middle ~10 minutes to allow oxidation to be measured. For several T_{NP} steps, the pre-oxidation period was omitted. The integrated emission intensity, I_{NP}, is also plotted. To show the behavior at low and high T_{NP} more clearly, **Fig. 2B** and **Fig. 2C** show magnified views of the 1400 - 1700 K, and 2100 - 2300 K ranges, respectively. **Fig. 2D** shows R_{oxid} and R_{base} for both heat ramps, calculated as described above, and plotted versus T_{NP}.

During the first heat ramp, the NP mass dropped by ~36%, from 55.5 MDa to ~34.7 MDa, while during the second ramp (**Fig. S5**) the mass dropped by an additional ~28%, to ~25.0 MDa. For reference, a spherical NP in this size range has a few percent of its atoms in the surface layer, thus on the order of 10 monolayers' worth of material was lost during each ramp. In the T_{NP} range up to 1800 K (**Fig. 2B**), the baseline mass loss rates in argon were slow, but increased dramatically when O_2 was added, similar to the behavior seen for the graphene NPs at low T_{NP}. Above 2000 K (**Fig. 2C**), the baseline rates in argon became quite large, but there was no obvious increase in slope when O_2 was added to the trap. The rates extracted from both heat ramps are summarized in **Fig. 2D**. R_{base} was found to increase sharply at T_{NP}, consistent with our observation that sublimation becomes fast for T_{NP} above ~1800 K.[3] The magnitudes of the area-normalized sublimation rates in the 2nd heat ramp were significantly lower than those in the 1st, and the T_{NP} dependence also changed. The R_{base} data above 1800 K in both heat ramps are well fit by Arrhenius

expressions of the form $R_{base} = A \cdot \exp(-E_a/kT_{NP})$, with best-fit activation energies (E_a) of ~379 kJ/mol for the 1st ramp and ~424 kJ/mol for the 2nd ramp. These are in the range of E_a values observed previously for sublimation of graphitic NPs,[3] and well below the ~862 kJ/mol E_a extracted from fitting bulk graphite sublimation rates.[68-71] As discussed previously,[3] the low E_a values, and the increase between the 1st and 2nd heat ramps, indicate that the NP initially had a large number of under-coordinated edge and defect sites that sublimed rapidly, but that the number of such sites decreased over the course of the experiment, as the NP lost mass due to the combination of oxidation and sublimation.

Fig. 2C also shows one additional point – that significant evolution of the NP surface site distribution can happen quickly, and in the absence of O_2. Note that each time T_{NP} was stepped 100 K to higher temperature, the mass loss rates, almost entirely due to sublimation in this T_{NP} range, were initially fast, but slowed significantly after just a few minutes. This implies that the surface site distribution evolved toward greater stability on the few minute time scale. Note that the R_{base} values shown in **Fig. 2D** for high T_{NP} (and used to calculate R_{oxid}), were taken as the mass loss rates *after* the fast initial sublimation periods, *i.e.*, R_{oxid} was calculated by subtracting the baseline rates just before and after O_2 was introduced.

R_{oxid} peaked for the 1st heat ramp at 1600 K, and decreased at higher T_{NP}, similar to the behavior observed for the graphene NP in **Fig. S3**. Because there was little change in mass loss slope when O_2 was introduced for $T_{NP} \geq 2100$ K, the subtraction at high T_{NP} is highly uncertain, and all we can really say is that R_{oxid} becomes much smaller than R_{base}. Similar decreases in oxidation rates were observed by Murray *et al.* for HOPG[14] and vitreous carbon surfaces,[63] and in their experiments they were able to see that the decrease in CO and CO_2 desorption at high surface

temperatures was accompanied by an increase in the competing O atom desorption channel. In our experiment, O or O_2 desorption is undetectable because they lead to no net mass change.

In the second heat ramp, the oxidation rate was near zero for T_{NP} < ~1800 K, rose to a peak around 2000 K, then fell to zero by 2200 K. Thus, the oxidation activity was much slower in the 2nd ramp at low temperatures, but similar at high temperatures. Again, the changes are attributed to evolution of the NP structure during the first heat ramp, such that there were fewer under-coordinated reactive sites.

Fig. 3 shows a more extreme example of decreasing NP reactivity over the course of an experiment. A somewhat larger graphite NP with 73.2 MDa initial mass was subjected to two stepwise heating ramps from 1600 K to 2100 K, *i.e.*, exploring a T_{NP} range intermediate to those in **Figs. 1-2**. The two heat ramps are shown in frames A and B, and the extracted R_{oxid} and R_{base} values are plotted versus T_{NP} in C. R_{base} was significant only for $T_{NP} \geq 1800$ K, as sublimation became fast. As in the previous examples, during the 1st heat ramp, R_{oxid} was much greater than R_{base} at low T_{NP}, but decreased at high T_{NP}, so that mass loss was

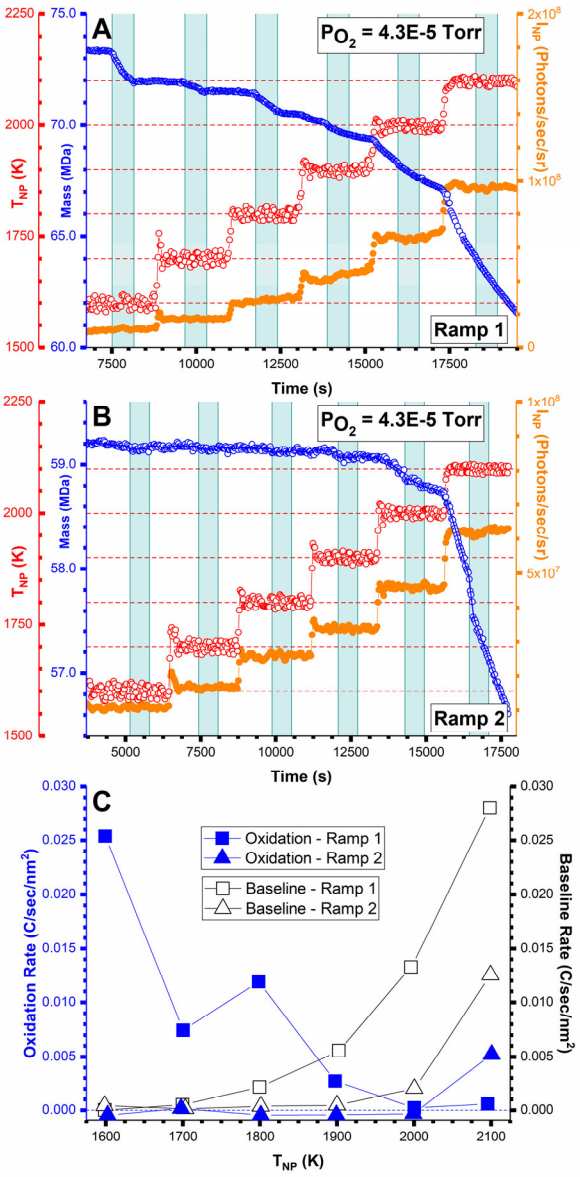

Figure 3: A). A 73.2 MDa graphite NP is ramped from 1600 K to 2100 K. B). A second T_{NP} ramp on the same NP. C). R_{oxid} and R_{base} for both ramps.

dominated by the rapidly growing sublimation rate. In the 2nd heat ramp, R_{base} was a factor of ~6.5 times lower than in the 1st ramp, but had similar T_{NP} dependence. In contrast, R_{oxid} was essentially zero in the 2nd ramp except at the highest T_{NP} (2100 K), where there was a short burst of fast mass loss when O_2 was first added (**Fig. 3B**), slowing to essentially the expected rate from sublimation alone after a few minutes. The dramatic decrease in oxidation activity is also clear from the total mass losses, which amounted to ~16.1 % (11.8 MDa), in the first heat ramp, but only ~4.4% (2.6 MDa) in the second ramp (almost entirely from sublimation), even though the T_{NP} range, times, and O_2 exposures were nearly identical.

One additional example of evolution of the surface reactivity for a graphite NP is given in **Fig. S6**, which shows a T_{NP} ramping experiment on a small, 23.2 MDa graphite NP in the 1500 – 2100 K range. In that experiment, the sublimation rates observed in both heat ramps are comparable to those measured for the other NPs in this T_{NP} range, but the oxidation rates showed two novel sorts of behavior. In the 1st heat ramp, and at most temperatures in the 2nd, the oxidation rates were quite low, albeit with T_{NP} dependence that was qualitatively similar to that for the other NPs. At two temperatures in the 2nd

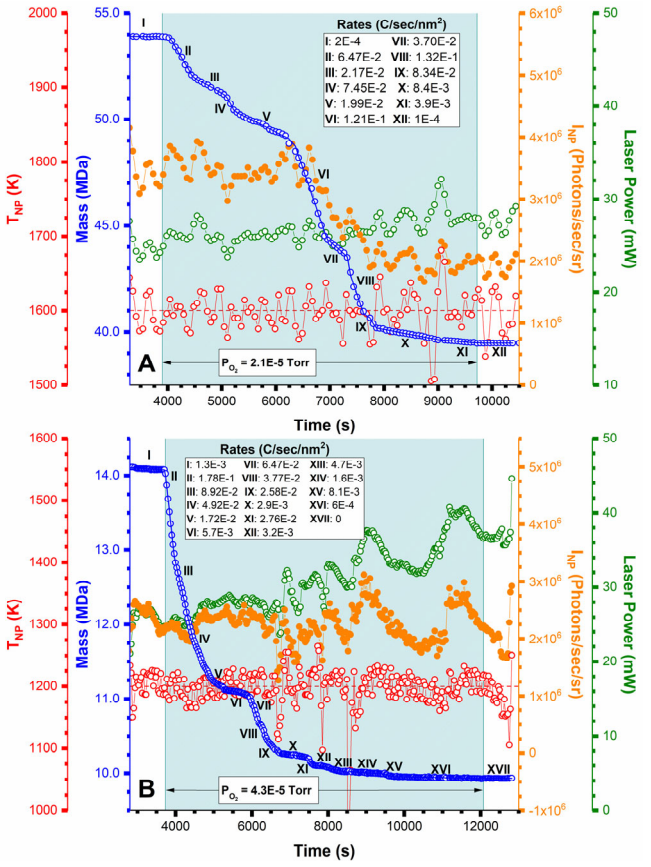

Figure 4: A). A 54.0 MDa graphite NP is held at 1600 K with P_{O2} = 2.1 x 10^{-5} Torr. B). A 14.1 MDa graphene NP held at 1200 K in 4.3 x 10^{-5} Torr of O_2.

heat ramp (1500 K and 1900 K), however, there were short periods when the oxidation rates increased dramatically with no change in T_{NP} or P_{O2}, by over an order of magnitude, preceded and/or followed by periods of very slow oxidation.

Oxidation at Constant T_{NP} and P_{O2}

The experiments discussed above provided evidence that the NP surface structure tended to evolve, sometimes dramatically, over the course of the experiments, slowing the sublimation and oxidation rates, particularly in experiments at higher temperatures. Those experiments varied T_{NP} and alternated periods with, and without O_2, complicating analysis of the dynamics of the surface structural evolution.

To allow the dynamic nature of the oxidation kinetics to be seen more clearly, we carried out simpler experiments of the type shown in **Fig. 4**, in which T_{NP} and P_{O2} were held constant for long time periods. **Fig. 4A** shows oxidation of a graphite NP with initial mass of 54.0 MDa that was trapped and charge stepped at low T_{NP} in 2.0 mTorr of Ar prior to the start of the record shown. T_{NP} was then set to 1600 K and the mass was monitored to establish the baseline mass loss rate, which was found to be near our detection limit. Next, O_2 was added to the trap at a partial pressure of 2.1×10^{-5} Torr (shaded background), and the NP was monitored for almost 6000 seconds, while it lost a total of 14.4 MDa, or ~27 % of its initial mass. At the end, the O_2 flow was stopped, to measure the final baseline mass loss rate, which also was near the detection limit.

The blue data points show the raw mass vs. time record, and the solid blue lines show a series of linear regressions used to fit the mass loss rates during periods when mass varied roughly linearly with time. The area-normalized rates (C/sec/nm^2) for the time periods labeled I through XII are given in the legend of the figure. These were determined from the linear fits, and have been normalized to the nominal surface areas in each time period, estimated from the NP mass

record. As above, the areas were calculated assuming spherical shape with the bulk graphite density. To obtain the R_{oxid} values given in the box in the figure, the total mass loss rate in each period was corrected by subtracting the baseline rate, estimated by interpolating between the baseline values measured at the beginning and end of the experiment. The baseline rates were generally small compared to the oxidation rates, even at the end, when the oxidation rate had fallen by a factor of ~20 from the initial rate.

T_{NP} was reasonably stable at 1600 ± 30 K (standard deviation), apart from a brief fluctuation of ~90 K at ~9000 seconds, near the end of the oxidation period. Nonetheless, the oxidation rate varied substantially, and non-monotonically. First note that there was a ~120 second induction period after O_2 was added to the trap, before significant mass loss began. Once started, the mass loss rate (*i.e.*, slope) varied non-monotonically by up to an order of magnitude, with relatively abrupt transitions between periods of faster or slower rates. Toward the end of the oxidation phase of the experiment (periods VIII-XI), the rates began to drop, eventually slowing to a rate >30 times smaller than the peak rate.

Fig. 4B shows a similar experiment for a 14.1 MDa graphene NP at significantly lower (1200 K) temperature, with P_{O2} roughly double the pressure used in **Fig. 4A**. The behavior was qualitatively similar. When O_2 was introduced, there was initially fast but non-monotonic oxidative mass loss, with periods of faster and slower rates, sometimes with quite abrupt transitions between them. Again, the oxidative mass loss rate eventually slowed, by a factor of ~300 in this case, dropping below the experimental sensitivity. The total mass loss observed before oxidation slowed dramatically was ~4 MDa, or ~28 % of the initial mass, which is similar to the ~27% mass loss observed the graphite NP in **Fig. 4A**. The integrated emission intensity remained nearly constant, with short term fluctuations that were correlated with fluctuations in heating laser power

and T_{NP}. Thus, the fluctuations are attributed to T_{NP} instabilities, rather than to any change in NP optical properties. Stabilizing such a low value of T_{NP} is challenging because the spectra are weak.

A final constant T_{NP}, constant P_{O2} experiment is summarized in **Fig. S7**, for a 32.6 MDa graphite NP held at 1700 K, and oxidized at 2.1 x 10^{-5} Torr of O_2. Because the temperature was higher, the initial oxidation rate, while still >20 times faster than the baseline rate, was significantly slower than the initial rates seen in **Fig. 4**, as might be expected from the heat ramp experiments, where oxidation rates generally decreased at higher T_{NP}. The oxidation rate in the 1700 K experiment fluctuated significantly, but less than in the 1600 K and 1200 K experiments, and in particular, the 1700 K experiment showed no sign of drastic slowing of the oxidation rate. The final rate was ~8 times lower than the initial rate, and this more modest slowing may simply reflect the fact that the percent mass loss was only a quarter of those in the experiments in **Fig. 4**, even though the oxidation period was substantially longer.

These experiments also provide insight into the evolution of the NP optical properties during oxidative mass loss. T_{NP} is determined by the balance between laser heating and cooling processes, including thermal radiation, Ar buffer gas collisions, and reaction exo/endothermicity. As discussed previously, thermal radiation dominates.[72] For example, a spherical 50 MDa graphitic NP at 1600 K would radiate ~4 x 10^{-11} W (2.5 x 10^8 eV/sec), even assuming a wavelength-averaged emissivity of only 0.02 (bulk graphite has emissivity of >0.9 in this temperature and wavelength range).[73] In contrast, Ar collisions would carry away at most ~1.2 x 10^{-12} W (7.5 x 10^6 eV/sec), and because the endo/exothermicity of sublimation and oxidation are on the order of a few eV *per* carbon atom lost, these reactions have negligible effects on the heat balance at the rates studied here.

Therefore, the energy balance required to hold the NP at fixed T_{NP} largely reflects the balance between absorption of the 532 nm heating laser and cooling by broadband emission. As a first approximation, we might expect both the 532 nm absorption cross section and broadband emission intensity to scale like the NP geometric cross section times the emissivity/absorptivity, which scattering theory[60] predicts should scale with NP radius for NPs much smaller than the wavelength emitted/absorbed. Thus considering only geometric factors, both the absorption cross section for heating, and the emission intensity for cooling would scale like the NP volume, and we might expect that heating and cooling should remain in balance as the NP shrinks. The sign of this situation would be constant heating laser power required to hold T_{NP} constant, and I_{NP} slowly declining proportional to the NP mass.

This expectation is correct in some cases, but in others, the actual behavior is more interesting. In **Fig. 4A**, for example, T_{NP} had good long term stability but I_{NP} did not simply decline slowly with NP mass, but rather was essentially constant as the NP lost ~15% of its initial mass, then dropped ~40% as the NP lost another ~10% of its mass, then stabilized again. Furthermore, the heating laser power had to be increased gradually throughout the experiment to hold T_{NP} constant, even during the period when I_{NP} (*i.e.*, the radiative cooling power) dropped by 40%. Clearly both the 532 nm absorption cross section and the broadband emissivity changed significantly, and differently, as the NP oxidized.

This behavior implies that the wavelength dependence of the emissivity must have changed during the experiment, and that is shown to be the case by **Fig. 5**. **Fig. 5A** compares raw spectra measured during time periods II and XI in **Fig. 4A**, *i.e.*, when O_2 was first introduced, and at the end of the oxidation period, when the oxidation rate was 16.6 times slower. The very different intensities reflect the ~40% drop in I_{NP} shown in **Fig. 4A**. **Fig. 5B** shows the same spectra

normalized at 1580 nm to allow the spectral shapes to be compared. Clearly, there is a significant difference in shape, with the period XI spectrum having higher curvature, which is also reflected by an increase in the best-fit n parameter to 1.78, compared to 1.36 for the early spectrum.

This result might suggest that NP optical properties are correlated with oxidation rates, however, the spectra in **Fig. 5C** show that this is not always the case. This figure compares the raw (un-normalized) spectra for periods II and XVI in **Fig. 4B**, *i.e.* immediately following O_2 addition, and at the end of the oxidation period, when the oxidation rate had dropped by a factor of ~300. In this example, the intensities, spectral shapes, and best-fit n parameters were nearly identical, even though the NP had lost a similar amount of mass to that in **Fig. 4A**, and the rate had slowed even more dramatically. Furthermore, despite the fact that I_{NP} (*i.e.*, the cooling power) was constant, apart from fluctuations due to T_{NP} stabilization problems, the laser intensity had to be increased by ~60%

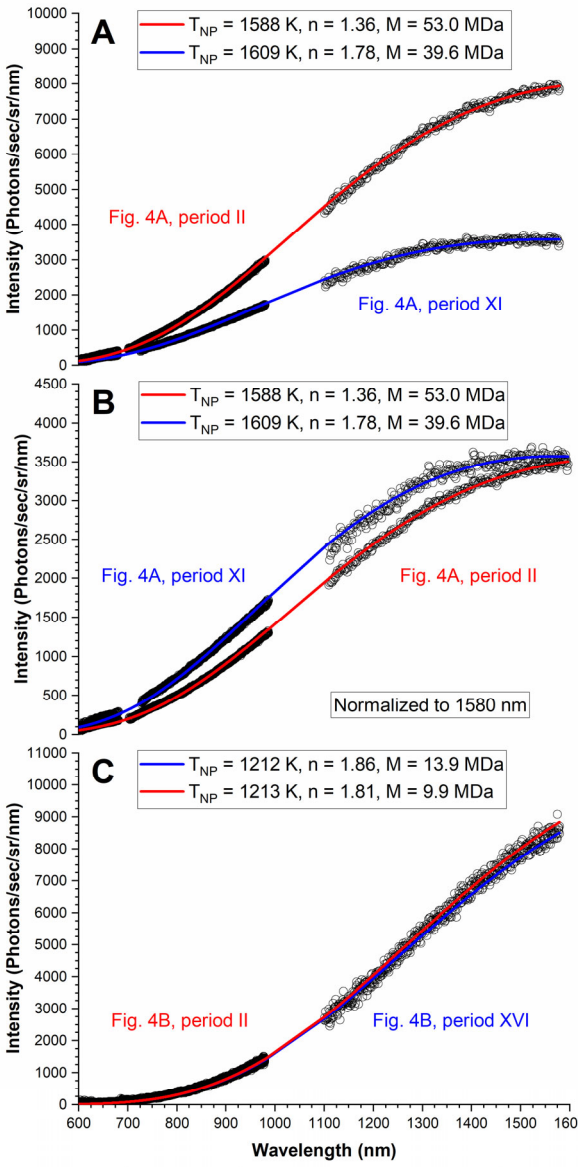

Figure 5: A). Spectra measured during periods II and XI in **Fig. 4A**, with fits, allowing n and T_{NP} to vary. B). The same spectra and fits normalized at 1580 nm. C). Spectra and fits from periods II and XVI of **Fig. 4B**.

to maintain T_{NP}, indicating that the 532 nm absorption cross section must have decreased relative to the broadband emissivity. **Fig. S7** and discussion thereof, present an example of yet another type of optical behavior, where I_{NP} *increased* by ~30% as the NP lost ~7% of its initial mass, but nonetheless, constant laser power was sufficient to maintain T_{NP}, indicating that the 532 nm absorption cross section must have also increased. The diversity of optical behavior observed in these oxidation experiments mirrors behavior seen during graphitic NP sublimation, mass loss by sublimation was sometimes accompanied by I_{NP} increasing, decreasing, or remaining unchanged,[1] but with a propensity for intensities to increase, while the sublimation rate slowed over time.[3] The variability of the optical effects is attributed to the same factors that cause the variability in oxidation and sublimation rates – *i.e.*, to NP-to-NP variations in the NP structure.

Effects on O_2 Oxidation from High T_{NP} Pre-Treatment

The experiments above showed both substantial NP-to-NP variations in oxidation behavior, and dramatic evolution of oxidation rates for individual NPs. The effects are attributed to NP-to-NP variations in the numbers of reactive surface sites, evolving as the NP loses carbon from its surface.

The experiments described above either heated the NPs to a series of increasing temperatures, alternating exposure to oxidizing and inert

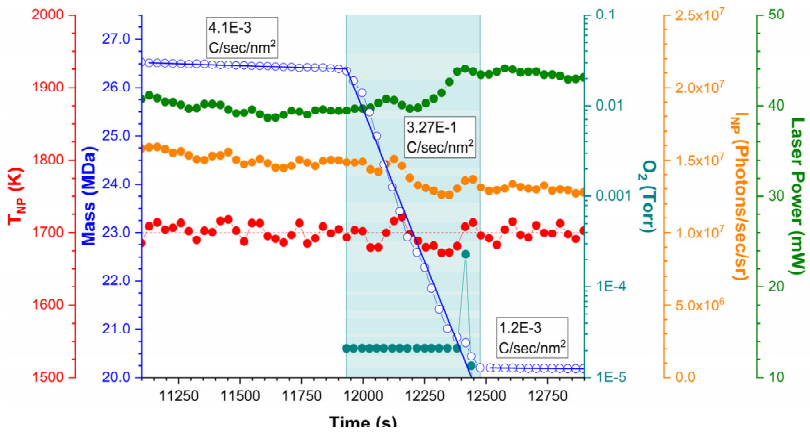

Figure 6: A 26.5 MDa graphite NP was annealed at T_{NP} >1900 K (not shown), then cooled to T_{NP} = 1700 K for measurements of R_{base} and R_{oxid}. I_{NP} and heating laser power are plotted in orange and green.

atmospheres, or simply held the NPs at constant T_{NP} and P_{O2}. **Figs. 6** and **S8** explore a third experimental protocol, in which the NPs were first pre-heated in inert atmosphere, then exposed to O_2 at lower T_{NP}, to look for effects of sublimation and annealing during the pre-heat period, on subsequent oxidation. **Fig. 6** shows results for a 26.5 MDa graphite NP. Prior to the start of the record shown, the NP was trapped at 1400 K, heated to $T_{NP} \approx 1900$ K for ~55 minutes, then cooled to ~1200 K to allow charge stepping. Charge stepping was done after the 1900 K pre-heat period because fast thermionic emission when NPs are first heated to high T_{NP} can make Q hard to track.

At the start of the experiment record shown in the figure, the NP was heated to 1700 K, and mass vs. time was tracked with the NP trapped in argon to obtain an initial baseline mass loss rate of $R_{base} = 4.1 \times 10^{-3}$ C/sec/nm^2. When O_2 was added at $P_{O2} = 2.1 \times 10^{-5}$ Torr (cyan background shading), there was an immediate increase in the mass loss rate by a factor of 80, and the rate remained nearly constant at an average, baseline-corrected value of ~3.3×10^{-1} C/sec/nm^2. During that period, the NP lost 6.1 MDa, corresponding to ~6 monolayers' worth of material. At ~12300 seconds, the rate began to slow slightly, and shortly thereafter, operator error caused a brief spike in P_{O2}. The O_2 was then shut off, for a measurement of the final baseline rate of 1.2×10^{-3} C/sec/nm^2, or ~1/3rd of the initial baseline rate.

While this is a simple experiment, there are some interesting points. First, the area-normalized oxidation rate (~3.3×10^{-1} C/sec/nm^2) was an order of magnitude faster than the fastest 1700 K rate observed in any of the graphite oxidation experiments described above, and roughly twice the fastest rates observed at any T_{NP}. The optical properties also were interesting. During the initial period at 1700 K prior to O_2 introduction, both the emission intensity, I_{NP}, and the laser power required to maintain T_{NP} decreased slowly with time, even though the NP mass was nearly constant. Then, as the NP rapidly lost mass after O_2 introduction, the laser power required to

maintain T_{NP} gradually increased, even though I_{NP}, *i.e.*, the cooling power, continued to decreased, indicating that the 532 nm absorption cross section decreased significantly during oxidation. Finally, when the O_2 was shut off, both resumed decreasing steadily.

Fig. S8 shows a more complicated experiment of this type with baseline and oxidation rates measured at 1500 K for a graphene NP with 86.9 MDa initial mass. The baseline rate was initially ~1.7 x 10^{-2} C/sec/nm^2, but after being briefly flashed to ~2050 K, R_{base} dropped by an order of magnitude. R_{oxid} was then measured to be 9.6 x 10^{-2} C/sec/nm^2 – faster than all but one of the NPs studied at 1500 K. The NP was then heated for 6 minutes to ~2050 K, and after re-cooling to 1500 K, R_{oxid} was found to have decreased by a factor of ~6.

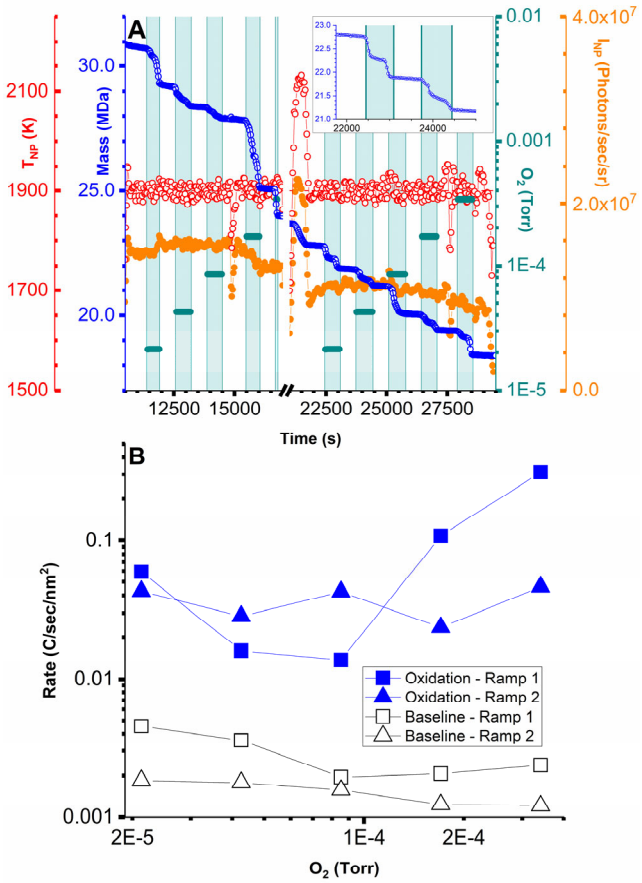

Figure 7: A). A 30.9 MDa graphite NP was held at 1900 K, then exposed to periods of increasing P_{O2}, annealed to 2100 K, then exposed to a 2nd P_{O2} ramp. B). R_{oxid} and R_{base} vs. P_{O2}. *Inset*) Expanded view of the 22000 to 25000 sec. range.

P_{O2} Dependence on Sublimation and Oxidation Rates at constant T_{NP}

The other obvious question is how the oxidation rates depend on the partial pressure of O_2. The simplest case would be an oxidation rate that is linear in P_{O2} and time-independent, however, the literature and the results shown above both suggest a more complex situation. As discussed in

the introduction, oxidation depends on the O_2 collision rate, but also on the O_2 dissociative adsorption probability and the decomposition branching ratios for the resulting oxygenated surface complexes. Because the energetics of the surface complexes depends on the local structure, and also on the presence of oxygen adsorbed nearby,[17, 21, 47, 54] the kinetics should be sensitive to oxygen coverage, resulting in a complex dependence on P_{O2}, T_{NP}, and time (due to evolution of the surface structure).

To probe the P_{O2} dependence, experiments of the type shown in **Fig. 7** were carried out. A graphite NP with 30.9 MDa initial mass was first charge stepped (not shown), and then T_{NP} was set to 1900 K and held constant. The NP was initially held in Ar for ~10 minutes to allow measurement of the baseline mass loss rate, mostly due to sublimation at this T_{NP}. O_2 was then added to the trap for 10 minute oxidation periods (shaded background) at a series of increasing P_{O2} values, with 10 minute Ar-only periods interspersed between each oxidation period to allow the baseline mass loss rate to be re-measured. P_{O2} started at 2.1 x 10^{-5} Torr and was doubled at each pressure step, up to 3.4 x 10^{-4} Torr, *i.e.*, a factor of ~16 increase. **Fig. 7B** plots the baseline rates (R_{base}) and the baseline-subtracted oxidation rates (R_{oxid}) associated with each P_{O2} step in the pressure ramps. The R_{base} values associated with each P_{O2} step were estimated from the mass loss rates during the Ar-only periods, averaging the slopes measured before and after each oxidation period. R_{oxid} values were calculated by subtracting R_{base} from the average mass loss rates during each oxidation period. Note that the R_{oxid} values are *not* normalized to P_{O2}, *i.e.*, if oxidative mass loss were linear in P_{O2}, the rate would increase a factor of ~2 for each P_{O2} step.

Instead, during the 1st P_{O2} ramp, R_{oxid} dropped by a factor of ~4 during the first three P_{O2} steps. Note, however, that R_{base} also dropped during this part of the experiment, by a factor ~2.5. At 1900 K, R_{base} is mostly due to sublimation, and in our study of graphitic NP sublimation

kinetics,[3] we observed significant drops in sublimation rate as the NPs were initially heated to drive loss of ~5% of their initial masses, with additional smaller rate decreases over time as the NPs continued to shrink. This slowing of the sublimation rates is attributed to evolution of the NP surface site distributions to have fewer of the defect and edge sites that contribute strongly to sublimation in this relatively low temperature regime. Such sites have also been shown to be important in oxidation of graphitic carbon by O_2 experimentally[4-11, 13, 31, 58, 64-66] and theoretically[16, 18, 20, 24-26, 28-29, 48, 54, 67] thus it is likely that the initial drop in oxidation rate as P_{O2} was increased was actually due to evolution of the NP surface structure as the NP lost ~10% of its initial mass (~3 monolayers' worth of material).

After the first few P_{O2} steps the sublimation rates stabilized, suggesting that the surface site evolution had slowed substantially. In contrast, the oxidation rate increased by a factor of almost 30 during the final three P_{O2} steps. Indeed, the rate during the final oxidation period (P_{O2} = 3.4 x 10^{-4} Torr) was so fast that it was terminated after only ~100 seconds to avoid burning up the NP. Because very fast mass loss makes it difficult to detect charge steps, which occur occasionally in this T_{NP} range, T_{NP} was then set to 1400 K to allow the charge to be re-measured (not shown).

Finally, the NP was held in argon for six minutes at 2100 K, and then a second 1900 K P_{O2} ramp was run to probe the effects on subsequent oxidation kinetics, from change caused by sublimation (and annealing) at 2100 K. During this 2nd P_{O2} ramp, the oxidation rates were in the same range as in the 1st ramp, but were nearly independent of P_{O2}. The baseline (*i.e.*, sublimation) rates were ~50% slower than during the 1st P_{O2} ramp, and declined slowly over the course of the 2nd P_{O2} ramp. The total mass loss during the 1st P_{O2} ramp was ~7 MDa, or ~22% of the initial mass, while in the 2nd P_{O2} ramp, ~4.5 MDa was lost, corresponding to ~20% of the NP mass at the start of ramp two. A further ~0.9 MDa was lost by sublimation during the 2100 K annealing period

between the P_{O2} ramps. The integrated emission intensity, I_{NP}, was relatively constant during the 1900 K portions of the experiment, with a slight initial increase, followed by decreases that can be at least partly attributed to shrinking of the emitting NP volume.

The inset to **Fig. 7** gives a magnified view of the period between 22000 to 25000 seconds, showing that the rate oscillated strongly even when T_{NP} and P_{O2} were constant. There were several periods of fast oxidation ($R_{oxid} \approx 10^{-1}$ C/sec/nm^2) during which 0.3 to 0.5 MDa was lost, interrupted by periods in which the mass was much slower. Close examination of the main figure shows similar, but smaller rate oscillations during other oxidation periods. For reference, note that a spherical NP with this mass would have *ca.* 4% of its mass in the surface monolayer, *i.e.*, the fluctuations occurred as the NP lost on the order of a monolayer's worth of material. Given that oxidation is expected to be dominated by O_2 reactions at under-coordinated edge/defect sites, such oscillations imply that the distribution of such sites can fluctuate substantially as the surface of an NP is reacted away.

Fig. S9 shows a similar P_{O2} ramping experiment, also at 1900 K, for a 73.0 MDa initial mass graphene NP. The graphene NP oxidative mass loss rate was in the same range as the rates observed for the graphite NP (**Fig. 7**), but the P_{O2} dependence was simpler. In both heat ramps, the rates increased with P_{O2} at low pressure, with weaker P_{O2} dependence at higher pressures. This NP also had periods in which the oxidation rates oscillated strongly at constant T_{NP} and P_{O2} during the 2nd P_{O2} ramp.

Fig. 8 shows a final example, where the behavior changed dramatically during the 2nd P_{O2} ramp. A graphene NP with initial mass 31.1 MDa was held at T_{NP} = 1500 K, and subjected to two P_{O2} ramps, separated by a period of annealing in argon. As with the previous examples, the baseline mass loss rate in argon was measured before and after each oxidation period to establish

R_{base}. During the inter-ramp period, the NP was heated above 1500 K for ~1000 seconds, however, as can be seen in the mass vs time record, fast sublimation occurred only during the ~350 second period when T_{NP} was ~2100 K. Mass tracking was lost during the high T_{NP} period due to fast sublimation and thermionic emission, therefore, charge stepping was repeated (break in time axis) prior to starting the 2nd P_{O2} ramp. The R_{oxid} and R_{base} values measured are summarized in **Fig. 8B**.

During the first heat ramp, P_{O2} was stepped from 2.1 x 10^{-5} to 1.7 x 10^{-4} Torr, resulting in loss of 4.4 MDa (~14% of the initial mass). When P_{O2} was initially doubled, R_{oxid} also approximately doubled, from 0.025 to 0.041 C/sec/nm^2, but then R_{oxid} was nearly P_{O2}-independent at higher pressures. The 1st ramp R_{oxid} values were in the same order of magnitude as the values in **Figs. 7** and **S9**. Note, however, that halfway through the final oxidation period of the 1st ramp, at

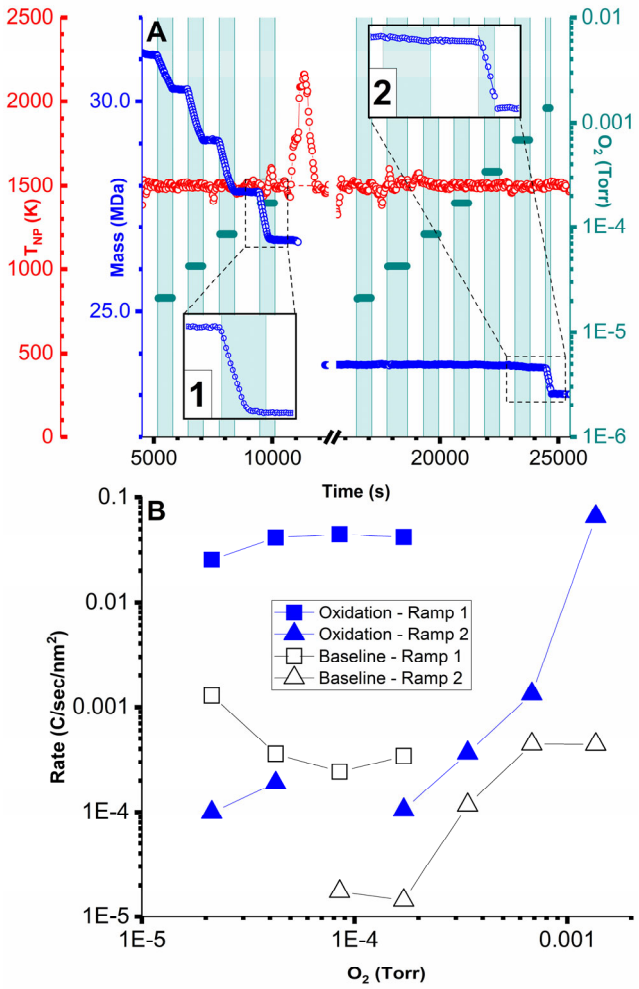

Figure 8: A). A 31.1 MDa graphene NP was heated to 1500 K, then subjected to two P_{O2} ramps with an annealing period in between. Insets show magnified views of two regions of the M vs. time record. B). R_{oxid} and R_{base} vs. P_{O2}. Missing points in the 2nd ramp data were zero within the experimental sensitivity.

~9820 seconds, the NP suddenly stopped losing mass even though T_{NP} and P_{O2} had not changed. A magnified view of the mass loss during this final oxidation period is shown in inset #1.

Despite having lost mass tracking during the 2100 K heating period, we can estimate the sublimation rate by recognizing that the rate should increase like $\exp(-E_a/kT_{NP})$, and therefore most of the mass lost during the gap in the mass record would have occurred during the 350 seconds at $T_{NP} \approx 2100$ K. This assumption gives an estimated ~2100 K sublimation rate of ~0.2 C/sec/nm^2, in reasonable agreement with the ~0.01 to ~0.15 C/sec/nm^2 sublimation rates previously observed for graphene NPs at 2100 K.[3] The point is that the abrupt decrease in oxidation reactivity at the end of the 1st P_{O2} ramp does not seem to have diminished the subsequent sublimation rate.

Thus, it was surprising to find that during the 2nd P_{O2} ramp, the NP was initially almost completely inert to O_2 for P_{O2} up to 1.7 x 10^{-4} Torr. To test this apparent inertness, the ramp was continued to higher O_2 pressures, with significant oxidative mass loss first observed at 6.8 x 10^{-4} Torr, and such fast oxidation at 1.36 x 10^{-3} Torr that oxidation had to be terminated quickly to avoid burning up the NP. A magnified view of the final two oxidation periods is shown in inset #2.

The conclusion is that something happened toward the end of the first P_{O2} ramp that abruptly rendered the NP surface nearly unreactive to O_2 at 1500 K, but still resulted in "normal" graphene NP sublimation during subsequent ~2100 K annealing. The annealed NP was essentially inert to O_2 during the first part of the 2nd P_{O2} ramp, but reactivity recovered as P_{O2} was increased, eventually exceeding the rates observed during the first P_{O2} ramp. Note that in **Fig. 7**, there were several similar abrupt decreases in oxidation rate during the 2nd P_{O2} ramp, but in each case the reactivity recovered spontaneously after a few minutes. Thus, it is unclear if the recovery of

reactivity in **Fig. 8** was driven by increasing P_{O2}, or would have occurred eventually at lower P_{O2}. Possible explanations for such drastic changes in reactivity will be discussed below.

Discussion

Fig. 9 assembles the kinetic information from the 14 experiments described above in a format intended to allow direct comparisons. Solid symbols denote results for graphene platelet NPs, with open symbols for graphite NPs. The figure includes the T_{NP} ramping ("heat ramp") experiments presented in **Figs. 1-3** and **S3-S6**, as well as the constant T_{NP}, constant P_{O2} experiments in **Figs. 4** and **S7**, the pre-heat experiments in **Figs. 6** and **S8**, and the P_{O2}-ramping experiments of **Figs. 7**, **8**, and **S9**. For clarity, only kinetics observed during the 1st heat ramp or P_{O2} ramp in those experiments are included. Data from the 2nd and 3rd heat ramps, and from the 2nd P_{O2} ramps on each NP are collected together in **Fig. S10**.

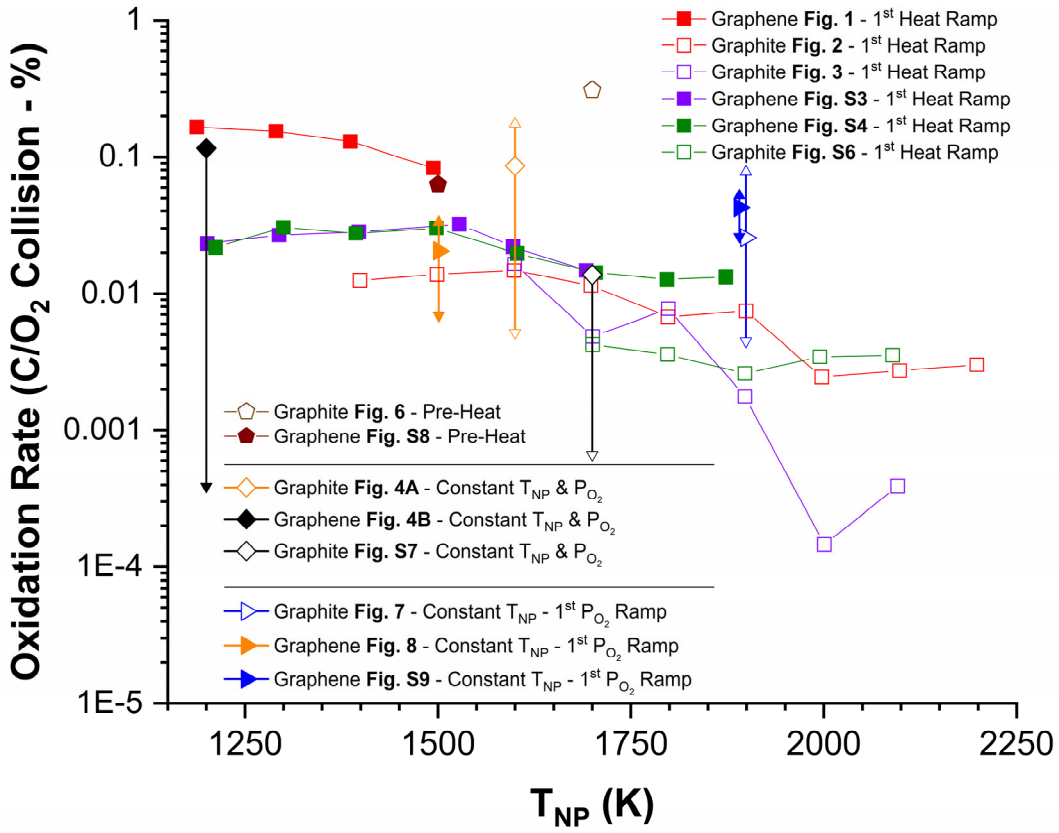

Figure 9: Oxidation efficiencies for all the NPs during the 1st T_{NP} ramp or P_{O2} exposure.

To allow comparison of experiments at different O_2 pressures, the rates have been converted to oxidation efficiencies (C atoms lost *per* O_2 collision), as follows. The values of P_{O2} were used to calculate the corresponding O_2 collision rates (O_2 collisions/second/nm^2), treating O_2 as an ideal gas with temperature equal to the trap temperature ≈ 300 K. This assumption is reasonable because at the total (Ar + O_2) pressures used, the mean free paths were always substantially larger than the trap size. The R_{oxid} values in the individual experiments (C/second/nm^2) were divided by the O_2 collision rates to obtain the oxidation efficiencies (C/O_2 collision). As with the oxidation rates, because we estimated the NP surface areas assuming spherical NP shape, the oxidation efficiencies are upper limits.

For the heat-ramp experiments, data points are shown for each T_{NP} examined in the 1st ramp for each NP. For the P_{O2}-ramp experiments, oxidation efficiencies were measured for a single T_{NP}, but for several different O_2 pressures, and a vertical double-ended arrow is used to show the range of oxidation efficiencies observed, with a symbol placed on each arrow to indicate the average efficiencies. P_{O2}-ramp experiments were done at 1900 K for both graphite and graphene NPs, and the associated symbols and arrows have been shifted slightly to higher and lower T_{NP} to avoid overlap. For the long duration, constant T_{NP}, constant P_{O2} experiments, oxidation was initially fast, fluctuated with time, and in two of the three experiments, the rates slowed dramatically at long times. In that situation, the average efficiency is ill defined, because it depends on how long the experiment was allowed run after the rates slowed. Therefore, for these experiments, the range of oxidation efficiencies is shown by a double-ended arrow, but the symbols placed on the arrows indicate the initial, rather than average efficiencies.

In the heat ramp experiments, the oxidation efficiencies for both graphite and graphene NPs tended to peak at low T_{NP}, dropping by roughly an order of magnitude as T_{NP} increased to

2000 K. Even within the heat ramp experiments on a particular NP type (*i.e.*, graphite, graphene), efficiencies varied from NP-to-NP by factors of 3 to 10. Furthermore, even for individual NPs, the rates varied substantially with time, generally slowing, but non-monotonically, as shown by the constant T_{NP}, constant P_{O2} experiments, but also by comparing data for the 1st, 2nd, and 3rd heat ramps (**Figs. 9** and **S10**). Similar NP-to-NP variations were observed in the initial sublimation rates for graphite and graphene NPs, studied using a heat ramp protocol, and the sublimation rates also slowed during repeated heat ramps, by factors ranging from ~7 at 1800 K to ~2 at 2100 K.[3] The NP-to-NP variations in sublimation rates were attributed to variations in distributions of NP surface sites, and the rate slowing was taken as the signature of evolution of the surface site distributions, driven by some combination of site-specific sublimation and annealing. Oxidation by O_2 is also expected to occur primarily at the same under-coordinated or defective sites that dominate sublimation,[9, 24, 28, 74] thus it is not surprising that oxidation and sublimation should have similar dependence on NP surface structure and its evolution.

In the heat ramp experiments and in some, but not all of the other experiments shown above, the initial oxidation efficiencies for graphene NPs tended to be two to three times higher than those for graphite NPs at the same temperatures, albeit with substantial NP-to-NP variability. Again, this is similar to the behavior seen for sublimation, where the area-normalized rates were observed to be higher for graphene, on average, compared to graphite NPs, with substantial NP-to-NP variations within each class of NPs. There are several factors that might be expected to affect the comparison of graphite and graphene NP kinetics. The first is an artifact. As noted, we assumed spherical shape in estimating the NP surface areas, which gives lower limits for the surface areas, hence upper limits for reaction rates and efficiencies. Clearly, this assumption is worse for graphene than graphite. To see how much worse, consider 50 MDa NPs with the

graphite bulk density but different shapes. A spherical NP would have diameter of ~41.2 nm, and surface area of ~5330 nm^2. An idealized "graphite" NP consisting of a cubical stack of basal plane layers would have 33.2 nm edge length, with total surface area of ~6600 nm^2, *i.e.*, ~25% larger than that of the sphere. For graphene platelet NPs, the equivalent model would be a thinner stack of square basal planes, with thickness equal to the average thickness reported for the graphene NP feedstock (5 nm). A 5 nm thick, square graphene platelet would have edge length of 85.5 nm, and total surface area of ~16,300 nm^2, roughly 3 times greater than the sphere, and ~2.5 times greater than the cube. Thus, the area-normalized rates and oxidation efficiencies for the graphite NPs are only modestly overestimated, but the overestimation for the graphene NPs is ~2.5 times larger, which would largely explain the higher apparent reactivity of the graphene NPs.

Experiments on HOPG and other bulk graphite materials[4-11, 13, 31, 58, 64-66] have shown, however, that in the low T_{NP} range where we observe the highest oxidation rates, perfect basal plane sites are unreactive, and oxidation by O_2 requires less stable sites. Such sites include basal plane defects, but NPs also have exposed basal plane edges that contain large numbers of under-coordinated sites. For the idealized cubical 50 MDa graphite NP, with basal planes on top and bottom faces, and two side faces each exposing zig-zag and armchair edges, the total number of exposed under-coordinated atoms (all the zig-zag, and half the armchair edge atoms) would be ~84,400, corresponding to ~42% of the total number of surface atoms. For the idealized 5 nm thick graphene platelet NP, the total surface area is ~2.5 times larger, but only ~11,000 under-coordinated edge atoms are exposed, corresponding to only ~2% of the total surface atoms. Thus, for idealized NPs that react only at edge sites, we would expect graphite NPs to be substantially more reactive than graphene NPs of the same mass, contrary to observations. The observation that the oxidation and sublimation kinetics for both graphene and graphite NPs are comparable, with

substantial NP-to-NP variations in both cases, reflects the fact that real graphitic NPs tend to be rough and irregular, and may have substantial numbers of basal plane defects, both factors tending to increase the number of exposed under-coordinated atoms.

Perhaps the most surprising observation in these oxidation experiments is that both graphite and graphene NPs tend to become almost inert after long periods of oxidation at $T_{NP} < 2000$ K. The evolution of the oxidation rate toward inertness is most clearly seen in the constant T_{NP}, constant P_{O2} experiments in **Fig. 4**, but rate decreases by factors of 10 or more, relative to the initial rate, were also observed in both the heat-ramp and P_{O2}-ramp experiments, particularly in the 2nd ramps (**Figs. 3**, **S4**, **8**)

As discussed above, previous work on O_2-oxidation of graphite and graphene has shown that perfect basal plane sites are unreactive, and that oxidation is dominated by reactions at defects and other strained or under-coordinated sites, such as exposed basal plane edges, and for rough or irregular NP structures, the numbers of such sites would be high. Since oxidation preferentially removes material from such sites, we might expect that asperities or irregularities in NP surfaces should tend to react away, reducing the numbers of reactive sites. To the extent that annealing is important for our time and temperature range, it also would tend to remove reactive sites, because such sites are also less energetically stable than fully coordinated sites. Therefore, it is unsurprising that oxidation efficiency (and sublimation rates[3]) should tend to decrease with time during reaction.

Transition to near-zero oxidation efficiency is, however, hard to explain within the graphitic structural motif, because, as outlined above, even idealized graphitic NPs would have substantial numbers of exposed reactive edge sites. The implication is that the inert NPs must have very few reactive surface sites, the obvious candidate is the carbon onion, or multi-wall fullerene

structure, in which the NP surface consists of concentric fully-coordinated fullerene-like shells. Formation of such NP has been observed after annealing to high temperatures for many different carbon nanomaterials,[75-77] including soot/carbon black[78-79] and nanodiamonds.[80-83] For soot/carbon black, temperatures in the 2500 to 2700 K are typically used to drive conversion to onion structures, but for nanodiamonds, spherical and polyhedral onion structures have been observed after annealing to 1800 - 2000 K for periods on the order of 20 minutes, *i.e.*, in range explored in our experiments. Formation of carbon onion NPs may explain also why initially trapped nanodiamonds were observed to give black-body-like emission spectra, almost indistinguishable from the spectra of black carbon NPs (graphite, graphene, carbon black).[1] It is not clear whether onion formation occurs for graphitic NPs under our conditions, however, this appears to be the most likely explanation for the transition to near-zero reactivity. Fast oxidation of partial shells, followed by slow oxidation of underlying complete shells might also account for examples where the oxidation rate oscillates substantially at constant T_{NP} and P_{O2} (*e.g.* **Fig. 7**, inset).

At this point, the idea that near-zero oxidation efficiency signals a transition to carbon onion structures is conjectural, however, we have some additional data bearing on this issue. In studies of sublimation of ~100 carbon NPs of various structures[1, 3] the sublimation rates are generally observed to slow with time, but typically only by factors of 5 to 8, even in experiments where the NP was held at high temperatures for >10 hours. This may indicate that onion structures do not form at the higher temperatures used in the sublimation study (1800 to 2100 K), or that onion structures are not stable with respect to sublimation at those temperatures. Because the transition to near-inert behavior is observed only after long times and substantial oxidative mass

loss, systematically exploring the factors that control the process is beyond the scope of the present study.

Conclusions

We have used several experimental protocols to study the O_2-oxidation kinetics of individual graphite and graphene NP as a function of T_{NP} and P_{O2}. The initial oxidation efficiencies were observed to peak in the 1200 to 1500 K range, falling by an order of magnitude as T_{NP} was increased to >2000 K. There were substantial variations in oxidation efficiencies from one NP to the next, and the efficiencies also decreased over time, non-monotonically, with substantial oscillations. NP-to-NP variations in efficiency are attributed to heterogeneity of the NP initial structures, with corresponding variations in the numbers of under-coordinated or defective sites exposed on the NP surfaces. The slow decreases in oxidation efficiency over time are attributed to evolution of the NP surface site distributions as the NPs lose mass, due to preferential etching of under-coordinated/defective sites. The more surprising observation was that in some cases, the NPs became essentially inert after a long period of oxidation. The cause of this behavior is uncertain, but a likely mechanism is formation of a fullerene-like surface layer that has few under-coordinated reactive sites.

Testing this hypothesis, and generating results for enough NPs to map out the distributions of reactivity and their evolution, will require an extensive set of experiments, which we are planning. The T_{NP}- and P_{O2}-ramping protocols will be used to study oxidation kinetics for large sets of individual graphite and graphene NPs, to map the NP-to-NP variations, and the T_{NP}, P_{O2}, and time dependence of the oxidation efficiencies. These experiments will also incorporate a single NP "titration" process that we are developing with the goal of being able to associate rates with numbers of exposed reactive sites. The long time behavior of the NPs will be studied to

obtain additional insight into the transition to nearly inert NPs under oxidizing conditions, but in addition, we plan experiments with carbon onion materials produced by annealing of nanodiamonds or carbon black, with electron microscopic verification of the feedstock structure. These more detailed studies, requiring many hundreds of hours of data acquisition, will require automation of essentially all aspects of the experiments and data analysis.

Methods

Measurement of NP mass and mass-loss kinetics

The instrument and methods for trapping single nanoparticles (NPs),[55] for spectroscopic NP temperature (T_{NP}) determination,[1-2] and for measuring reaction kinetics,[3] have been described in detail elsewhere. In short, electrospray ionization (ESI) is used to inject NPs into the instrument vacuum system, where they are collected by a radio-frequency (rf) hexapole that guides them through a differential pumping region. They are then focused through an isolation valve, into an rf quadrupole that guides them to a split-ring-electrode quadrupole trap (SRET),[56] where the NP beam is injected along the trap axis. Lasers can be focused through the trap center along two orthogonal axes, while light emitted by a trapped NP is focused onto an avalanche photodiode (APD) module (*Laser Components*), sensitive to wavelengths (λ) < ~1000 nm. In a typical experiment, a CO_2 laser is focused through the trap with a >1 mm beam waist as the NP beam is injected. To aid trapping, the trap pressure is set to ~15 mTorr of argon (UHP grade), and the frequency (F_{RF}) and amplitude (V_0) of the bipolar potential applied to the trap are set to ~25 kHz and ~350 V, respectively. When an NP becomes trapped, the laser heats it to incandescence, which is detected by the APD, and the CO_2 laser and NP beams are automatically shut off. Once an NP is trapped, the argon pressure is dropped to 2.0 mTorr, and heating is done using a cw 532 nm laser, which provides better T_{NP} control. We previously tested the effects of heating laser

wavelength (532 nm vs. 10.6 μm) on the emission spectra and sublimation rates for a variety of carbon NPs,[1] finding no significant differences for any given T_{NP}.

An NP with mass (M) and charge (Q) oscillates in the trap with well-defined frequencies associated with axial and radial motion.[56] The axial frequency (F_z) is given by Eqn. 1

$$F_z = \left(\frac{Q}{M}\right)\left(\frac{\sqrt{2}V_0}{4\pi^2 F_{RF} z_0^2}\right), \qquad (1)$$

where the geometric parameter (z_0) is estimated to be 2.96 mm for our trap. F_z is measured every 30 to 60 seconds using a resonance excitation method,[57] in which the frequency of a weak AC "drive" potential applied to an electrode just outside the trap is swept. When the drive is resonant with F_z, the amplitude of axial motion becomes large enough to reduce the collection efficiency of the APD, resulting in a sharp dip in emission signal (see inset to **Fig. S1**). To obtain M from F_z, it is necessary to know Q, which is determined by a charge stepping process, illustrated in the initial section of **Fig. S1**. A vacuum UV lamp is used to induce a series of single e^- changes in Q due to photoemission from the NP or capture of electrons photoemitted from trap surfaces. These charge steps appear as steps in F_z which are fit to obtain Q. For Q < 50 e, it is generally possible to determine Q exactly, while for large NPs, which tend to have Q > 50 e, there is ~±1% uncertainty in the extracted Q value.

Kinetics for mass-changing reactions, such as sublimation or oxidation, are measured simply by measuring M vs. time as the NP is heated to some T_{NP} of interest, in either inert or reactive atmosphere. Rates are determined by fitting a series of typically ~20 mass measurements. **Fig. S1** shows an example of measuring F_z vs. time, using charge stepping to find Q, and determining M vs. time for a simple kinetics experiment. For NPs with Q < 50 e, the main source of uncertainty in the mass measurements, hence the reaction rates, is the z_0 parameter, which depends on the construction accuracy of the trap. We estimate that the absolute mass uncertainty

from this factor is ~±1.3%. For NPs with higher Q, the uncertainty in Q adds an additional ~1% uncertainty in the absolute mass. The relative uncertainty in comparing masses is much better, estimated to be ~±0.2%, resulting from the combined measurement accuracies for F_z, F_{RF}, and V_0.

It is important that the NP surfaces be clean, particularly avoiding metal contaminants that might catalyze oxidation of the NP. The graphite NP feedstock (*Alfa Aesar*) is natural graphite with purity of 99.9999% (metals basis), and the graphene platelet material (*US Research Nanomaterials*) has stated composition of 99.7% C, <0.3% O. The graphene thickness is given as 2 to 8 nm, *i.e.*, the 5 nm average thickness corresponds to ~15 graphene layers. The graphite NPs were prepared by first grinding ~200 mg of the 200 mesh feedstock using a polished agate mortar and pestle, then dispersing it by ultrasonication in 20 mL of HPLC grade methanol in a 20 mL glass scintillation vial. The electrospray (ESI) solution was prepared by mixing 1 mL of the graphite/methanol suspension with 3 mL of ~2 mM ammonium acetate/methanol solution. The graphene NP suspension was prepared by simply sonicating the feedstock in methanol for a few minutes, then mixing with the ammonium acetate/methanol solution. The electrosprayed NPs likely have adsorbed ammonium acetate, methanol, and possibly atmospheric water, and because the feedstocks were handled in air, the NPs presumably also have surface functional groups containing O, H, or N atoms. Such contaminants are not problematic, because they are known[9, 33-34, 58-59] to decompose/desorb at relatively low temperatures. Because our NPs are initially held for charge stepping at T_{NP} > 1300 K for at least 20 minutes, we expect that the surfaces are essentially pure carbon at the start of the kinetics experiments.

Measurement of NP temperature (T_{NP})

To obtain T_{NP} to associate with the rates, we use an optical system and calibration methods that have been described in detail elsewhere.[1-2] Emission is collected, split into "visible" (λ < 980

nm) and "nIR" (λ > 980 nm) beams, and dispersed by a pair of spectrographs, thus allowing measurement of spectra in the 600 to 1600 nm range, simultaneous with each NP mass measurement. Example spectra at several different T_{NP} values are shown in **Fig. S2**. To obtain T_{NP} from the spectra, they are fit to a thermal emission model consisting of Planck's law for ideal black body emission, times an emissivity function, $\epsilon(\lambda,T_{NP})$, which describes non-idealities due to the small size of the NP compared to λ, the optical properties of the NP material, and the effects of surface or other localized states on the NP emission properties. As detailed elsewhere,[1] the correct form of $\epsilon(\lambda,T_{NP})$ is unknown, and here it is approximated by a power law function: $\epsilon(\lambda,T_{NP}) \propto \lambda^{-n}$. With this approximation, the emission model function is:

$$I(\lambda, T_{NP}) = \frac{K}{\lambda^{(4+n)}.\left(exp\left(\frac{hc}{\lambda k_b T_{NP}}\right)-1\right)}, \qquad (2)$$

where K is just a normalization constant, and the shape of the function depends on just the T_{NP} and n parameters. As shown in **Fig. S2**, this model provides adequate fits to the measured spectra, and as detailed previously,[1] we estimate that the T_{NP} values thus obtained have absolute uncertainty of ~6.7%, with ~2% relative uncertainty associated with comparing T_{NP}s extracted by fitting similar spectra. In addition to providing temperature to associate with rates, the T_{NP} values extracted from the spectra are used to stabilize T_{NP} by adjusting the intensity of the 532 nm heating laser.

Acknowledgments

The nIR spectrograph was purchased with funds from the Albaugh Scientific Equipment Endowment of the College of Science, University of Utah. This material is based upon work supported by the U.S. Department of Energy, Office of Science, Office of Basic Energy Sciences,

under Award Number DE-SC-0018049. We thank Prof. T. Minton (Montana State University) for helpful discussions.

Supporting Information

The Supporting Information is available free of charge via the Internet at http://pubs.acs.org.

The following files are available free of charge: **Figures S1-S9** show examples of raw experiment data, additional spectra with fits, and additional examples of oxidation rates measured under different reaction protocols. Data underlying **Figures 1-9** are provided in tabular form (XLSX).

REFERENCES

1. Long, B. A.; Rodriguez, D. J.; Lau, C. Y.; Schultz, M.; Anderson, S. L., Thermal Emission Spectroscopy of Single, Isolated Carbon Nanoparticles: Effects of Particle Size, Material, Charge, Excitation Wavelength, and Thermal History. *J. Phys. Chem. C* **2020,** *124*, 1704-1716.

2. Long, B. A.; Rodriguez, D. J.; Lau, C. Y.; Anderson, S. L., Thermal emission spectroscopy for single nanoparticle temperature measurement: optical system design and calibration. *Appl. Opt.* **2019,** *58* (3), 642-649.

3. Long, B. A.; Lau, C. Y.; Rodriguez, D. J.; Tang, S. A.; Anderson, S. L., Sublimation Kinetics for Individual Graphite and Graphene Nano-particles (NPs): NP-to-NP Variations and Evolving Structure-Kinetics and Structure-Emissivity Relationships. *J. Am. Chem. Soc.* **2020,** *(on line 7/22/2020)*.

4. Olander, D. R.; Jones, R. H.; Schwarz, J. A.; Siekhaus, W. J., Reactions of Modulated Molecular Beams with Pyrolytic Graphite. II Oxidation of the Prism Plane. *The Journal of Chemical Physics* **1972,** *57* (1), 421-433.

5. Olander, D. R.; Siekhaus, W.; Jones, R.; Schwarz, J. A., Reactions of Modulated Molecular Beams with Pyrolytic Graphite. I. Oxidation of the Basal Plane. *J. Chem. Phys.* **1972,** *57* (1), 408-420.

6. Barber, M.; Evans, E. L.; Thomas, J. M., Oxygen chemisorption on the basal faces of graphite: an XPS study. *Chemical Physics Letters* **1973,** *18* (3), 423-425.

7. Chang, H.; Bard, A. J., Formation of monolayer pits of controlled nanometer size on highly oriented pyrolytic graphite by gasification reactions as studied by scanning tunneling microscopy. *J. Am. Chem. Soc.* **1990,** *112* (11), 4598-9.

8. Chu, X.; Schmidt, L. D., Reactions of NO, O2, H2O, and CO2 with the basal plane of graphite. *Surface Science* **1992,** *268* (1), 325-332.

9. Nowakowski, M. J.; Vohs, J. M.; Bonnell, D. A., Surface reactivity of oxygen on cleaved and sputtered graphite. *Surf. Sci.* **1992,** *271* (3), L351-L356.

10. Stevens, F.; Kolodny, L. A.; Beebe, T. P., Jr., Kinetics of Graphite Oxidation: Monolayer and Multilayer Etch Pits in HOPG Studied by STM. *J. Phys. Chem. B* **1998,** *102* (52), 10799-10804.

11. Hahn, J. R., Kinetic study of graphite oxidation along two lattice directions. *Carbon* **2005,** *43* (7), 1506-1511.

12. Nicholson, K. T.; Minton, T. K.; Sibener, S. J., Spatially Anisotropic Etching of Graphite by Hyperthermal Atomic Oxygen. *The Journal of Physical Chemistry B* **2005,** *109* (17), 8476-8480.

13. Edel, R.; Grabnic, T.; Wiggins, B.; Sibener, S. J., Atomically-Resolved Oxidative Erosion and Ablation of Basal Plane HOPG Graphite Using Supersonic Beams of O2 with Scanning Tunneling Microscopy Visualization. *The Journal of Physical Chemistry C* **2018,** *122* (26), 14706-14713.

14. Murray, V. J.; Smoll, E. J.; Minton, T. K., Dynamics of Graphite Oxidation at High Temperature. *J. Phys. Chem. C* **2018,** *122* (12), 6602-6617.

15. Montoya, A.; Truong, T.-T. T.; Mondragón, F.; Truong, T. N., CO Desorption from Oxygen Species on Carbonaceous Surface: 1. Effects of the Local Structure of the Active Site and the Surface Coverage. *The Journal of Physical Chemistry A* **2001,** *105* (27), 6757-6764.

16. Sorescu, D. C.; Jordan, K. D.; Avouris, P., Theoretical Study of Oxygen Adsorption on Graphite and the (8,0) Single-walled Carbon Nanotube. *The Journal of Physical Chemistry B* **2001,** *105* (45), 11227-11232.

17. Montoya, A.; Mondragón, F.; Truong, T. N., First-Principles Kinetics of CO Desorption from Oxygen Species on Carbonaceous Surface. *The Journal of Physical Chemistry A* **2002,** *106* (16), 4236-4239.

18. Montoya, A.; Mondragón, F.; Truong, T. N., Formation of CO precursors during char gasification with O2, CO2 and H2O. *Fuel Processing Technology* **2002,** *77-78*, 125-130.

19. Frankcombe, T. J.; Smith, S. C., On the microscopic mechanism of carbon gasification: A theoretical study. *Carbon* **2004,** *42* (14), 2921-2928.

20. Xu, Y.-J.; Li, J.-Q., The interaction of molecular oxygen with active sites of graphite: a theoretical study. *Chemical Physics Letters* **2004,** *400* (4), 406-412.

21. Sendt, K.; Haynes, B. S., Density Functional Study of the Reaction of Carbon Surface Oxides: The Behavior of Ketones. *The Journal of Physical Chemistry A* **2005,** *109* (15), 3438-3447.

22. Li, J.-L.; Kudin, K. N.; McAllister, M. J.; Prud'homme, R. K.; Aksay, I. A.; Car, R., Oxygen-Driven Unzipping of Graphitic Materials. *Physical Review Letters* **2006,** *96* (17), 176101.

23. Sánchez, A.; Mondragón, F., Role of the Epoxy Group in the Heterogeneous CO2 Evolution in Carbon Oxidation Reactions. *The Journal of Physical Chemistry C* **2007,** *111* (2), 612-617.

24. Carlsson, J. M.; Hanke, F.; Linic, S.; Scheffler, M., Two-Step Mechanism for Low-Temperature Oxidation of Vacancies in Graphene. *Physical Review Letters* **2009,** *102* (16), 166104.

25. Radovic, L. R., Active Sites in Graphene and the Mechanism of CO2 Formation in Carbon Oxidation. *Journal of the American Chemical Society* **2009,** *131* (47), 17166-17175.

26. Morón, V.; Gamallo, P.; Sayós, R., DFT and kinetics study of O/O2 mixtures reacting over a graphite (0001) basal surface. *Theoretical Chemistry Accounts* **2011,** *128* (4), 683-694.

27. Poovathingal, S.; Schwartzentruber, T. E.; Srinivasan, S. G.; van Duin, A. C. T., Large Scale Computational Chemistry Modeling of the Oxidation of Highly Oriented Pyrolytic Graphite. *The Journal of Physical Chemistry A* **2013,** *117* (13), 2692-2703.

28. Hariharan, S.; Majumder, M.; Edel, R.; Grabnic, T.; Sibener, S. J.; Hase, W. L., Exploratory Direct Dynamics Simulations of $^3O_2$ Reaction with Graphene at High Temperatures. *The Journal of Physical Chemistry C* **2018,** *122* (51), 29368-29379.

29. Majumder, M.; Gibson, K. D.; Sibener, S. J.; Hase, W. L., Chemical Dynamics Simulations and Scattering Experiments for O2 Collisions with Graphite. *The Journal of Physical Chemistry C* **2018,** *122* (28), 16048-16059.

30. Hahn, J. R.; Kang, H., Conversion efficiency of graphite atomic-scale defects to etched pits in thermal oxidation reaction. *J. Vac. Sci. Technol., A* **1999,** *17* (4, Pt. 1), 1606-1609.

31. Lee, S. M.; Lee, Y. H.; Hwang, Y. G.; Hahn, J. R.; Kang, H., Defect-Induced Oxidation of Graphite. *Physical Review Letters* **1999,** *82* (1), 217-220.

32. Britten, J. A.; Falconer, J. L.; Brown, L. F., Effect of nonreacting gases on the desorption of reaction-created CO from graphite. *Carbon* **1985,** *23* (6), 627-633.

33. Marchon, B.; Carrazza, J.; Heinemann, H.; Somorjai, G. A., TPD and XPS studies of O2, CO2, and H2O adsorption on clean polycrystalline graphite. *Carbon* **1988,** *26* (4), 507-514.

34. Pan, Z.; Yang, R. T., Strongly Bonded Oxygen in Graphite: Detection by High-Temperature TPD and Characterization *Ind. Eng. Chem. Res.* **1992,** *31*, 2675-2680.

35. Ma, M. C.; Brown, T. C.; Haynes, B. S., Evaluation of thermal desorption spectra for heterogeneous surfaces: application to carbon surface oxides. *Surface Science* **1993,** *297* (3), 312-326.

36. Ma, M. C.; Haynes, B. S., Surface heterogeneity in the formation and decomposition of carbon surface oxides. *Symposium (International) on Combustion* **1996,** *26* (2), 3119-3125.

37. Zhuang, Q.; Kyotani, T.; Tomita, A., Desorption Behavior of Surface Oxygen Complexes on Carbon in an Inert Gas and in O2-Gasification Atmosphere. *Energy Fuels* **1996,** *10* (1), 169-172.

38. Haydar, S.; Moreno-Castilla, C.; Ferro-García, M. A.; Carrasco-Marín, F.; Rivera-Utrilla, J.; Perrard, A.; Joly, J. P., Regularities in the temperature-programmed desorption spectra of CO2 and CO from activated carbons. *Carbon* **2000,** *38* (9), 1297-1308.

39. Haynes, B. S.; Newbury, T. G., Oxyreactivity of carbon surface oxides. *Proc. Combust. Inst.* **2000,** *28* (2), 2197-2203.

40. Sibraa, A.; Newbury, T.; Haynes, B. S., The reactions of hydrogen and carbon monoxide with surface-bound oxides on carbon. *Combust. Flame* **2000,** *120* (4), 515-525.

41. Boehm, H. P., Surface oxides on carbon and their analysis: a critical assessment. *Carbon* **2002,** *40* (2), 145-149.

42. Kwon, S.; Vidic, R.; Borguet, E., Enhancement of adsorption on graphite (HOPG) by modification of surface chemical functionality and morphology. *Carbon* **2002,** *40* (13), 2351-2358.

43. Incze, A.; Pasturel, A.; Chatillon, C., Oxidation of graphite by atomic oxygen: a first-principles approach. *Surface Science* **2003,** *537* (1), 55-63.

44. Kwon, S.; Vidic, R.; Borguet, E., The effect of surface chemical functional groups on the adsorption and desorption of a polar molecule, acetone, from a model carbonaceous surface, graphite. *Surf. Sci.* **2003,** *522* (1–3), 17-26.

45. Montoya, A.; Mondragón, F.; Truong, T. N., CO2 adsorption on carbonaceous surfaces: a combined experimental and theoretical study. *Carbon* **2003,** *41* (1), 29-39.

46. Zhu, Z.; Lu, G. Q.; Finnerty, J.; Yang, R. T., Electronic structure methods applied to gas–carbon reactions. *Carbon* **2003,** *41* (4), 635-658.

47. Espinal, J. F.; Montoya, A.; Mondragón, F.; Truong, T. N., A DFT Study of Interaction of Carbon Monoxide with Carbonaceous Materials. *The Journal of Physical Chemistry B* **2004,** *108* (3), 1003-1008.

48. Allouche, A.; Ferro, Y., Dissociative adsorption of small molecules at vacancies on the graphite (0001) surface. *Carbon* **2006,** *44* (15), 3320-3327.

49. Cabrera-Sanfelix, P.; Darling, G. R., Dissociative Adsorption of Water at Vacancy Defects in Graphite. *J. Phys. Chem. C.* **2007,** *111* (49), 18258-18263.

50. Barinov, A.; Malcioğlu, O. B.; Fabris, S.; Sun, T.; Gregoratti, L.; Dalmiglio, M.; Kiskinova, M., Initial Stages of Oxidation on Graphitic Surfaces: Photoemission Study and Density Functional Theory Calculations. *The Journal of Physical Chemistry C* **2009,** *113* (21), 9009-9013.

51. Orrego, J. F.; Zapata, F.; Truong, T. N.; Mondragón, F., Heterogeneous CO2 Evolution from Oxidation of Aromatic Carbon-Based Materials. *The Journal of Physical Chemistry A* **2009,** *113* (29), 8415-8420.

52. Xu, S. C.; Irle, S.; Lin, M. C., Quantum Chemical Prediction of Reaction Pathways and Rate Constants for Reactions of NO and NO2 with Monovacancy Defects on Graphite (0001) Surfaces. *J. Phys. Chem. C* **2010,** *114* (18), 8375-8382.

53. Yamada, Y.; Yasuda, H.; Murota, K.; Nakamura, M.; Sodesawa, T.; Sato, S., Analysis of Heat-Treated Graphite Oxide by X-ray Photoelectron Spectroscopy. *J. Mater. Sci.* **2013,** *48*, 8171-8198.

54. Chen, N.; Yang, R. T., Ab Initio Molecular Orbital Study of the Unified Mechanism and Pathways for Gas−Carbon Reactions. *The Journal of Physical Chemistry A* **1998,** *102* (31), 6348-6356.

55. Howder, C. R.; Bell, D. M.; Anderson, S. L., Optically Detected, Single Nanoparticle Mass Spectrometer With Pre-Filtered Electrospray Nanoparticle Source. *Rev. Sci. Instrum.* **2014,** *85*, 014104 -014110.

56. Schlemmer, S.; Illemann, J.; Wellert, S.; Gerlich, D., Nondestructive High-Resolution And Absolute Mass Determination Of Single Charged Particles In A Three-Dimensional Quadrupole Trap. *J. Appl. Phys.* **2001,** *90* (10), 5410-5418.

57. Bell, D. M.; Howder, C. R.; Johnson, R. C.; Anderson, S. L., Single CdSe/ZnS Nanocrystals in an Ion Trap: Charge and Mass Determination and Photophysics Evolution with Changing Mass, Charge, and Temperature. *ACS Nano* **2014,** *8*, 2387–2398.

58. Tremblay, G.; Vastola, F. J.; Walker, P. L., Jr., Characterization of Graphite Surface Complexes by Temperature-Programmed Desorption. *Extended Abstracts - Bienneial Conf. on Carbon* **1975,** *12*, 177-178.

59. Olszak-Humienik, M., On the thermal stability of some ammonium salts. *Thermochim. Acta* **2001,** *378* (1), 107-112.

60. Bohren, C. F.; Huffman, D. R., *Absorption and Scattering of Light by Small Particles*. Wiley: New York, 1983.

61. Bacon, G. E., The interlayer spacing of graphite. *Acta Crystallogr. A* **1951,** *4* (6), 558-561.

62. Laine, N. R.; Vastola, F. J.; Walker, P. L., The Importance of Active Surface Area in the Carbon-Oxygen Reaction. *J. Phys. Chem.* **1963,** *67* (10), 2030-2034.

63. Murray, V. J.; Marshall, B. C.; Woodburn, P. J.; Minton, T. K., Inelastic and Reactive Scattering Dynamics of Hyperthermal O and O_2 on Hot Vitreous Carbon Surfaces. *J. Phys. Chem. C* **2015,** *119*, 14780-14796.

64. Rosner, D. E.; Allendorf, H. D., Comparative studies of the attack of pyrolytic and isotropic graphite by atomic and molecular oxygen at high temperatures. *AIAA Journal* **1968,** *6* (4), 650-654.

65. Walls, J. R.; Strickland-Constable, R. F., Oxidation of Carbon between 1000 - 2400 C. *Carbon* **1964,** *1*, 333-338.

66. McCarroll, B.; McKee, D. W., Reactivity of graphite surfaces with atoms and molecules of hydrogen, oxygen, and nitrogen. *Carbon* **1971,** *9* (3), 301-311.

67. Chen, S. G.; Yang, R. T.; Kapteijn, F.; Moulijn, J. A., A new surface oxygen complex on carbon: toward a unified mechanism for carbon gasification reactions. *Industrial & Engineering Chemistry Research* **1993,** *32* (11), 2835-2840.

68. Clarke, J. T.; Fox, B. R., Rate and Heat of Vaporization of Graphite above 3000°K. *J. Chem. Phys.* **1969,** *51* (8), 3231-3240.

69. Marshall, A. L.; Norton, F. J., Carbon Vapor Pressure and Heat of Vaporization. *J. Am. Chem. Soc.* **1950,** *72* (5), 2166-2171.

70. Tsai, C. C.; Gabriel, T. A.; Haines, J. R.; Rasmussen, D. A., Graphite Sublimation Tests For Target Development For The Muon Collider/Neutrino Factory *IEEE Symp. Fusion Eng.* **2006,** *21*, 377-379.

71. Haines, J. R.; Tsai, C. C. *Graphite Sublimation Tests for the Muon Collider/Neutrino Factory Target Development Program*; Oak Ridge, 2002; p 6 pages.

72. Howder, C. R.; Long, B. A.; Alley, R. N.; Gerlich, D.; Anderson, S. L., Single Nanoparticle Mass Spectrometry as a High Temperature Kinetics Tool: Emission Spectra, Sublimation, and Oxidation of Hot Carbon Nanoparticles. *J. Phys. Chem. A* **2015,** *119*, 12538–12550.

73. Neuer, G., Spectral and total emissivity measurements of highly emitting materials. *Int. J. Thermophys.* **1995,** *16* (1), 257-265.

74. Hahn, J. R.; Kang, H.; Lee, S. M.; Lee, Y. H., Mechanistic Study of Defect-Induced Oxidation of Graphite. *J. Phys. Chem. B* **1999,** *103* (45), 9944-9951.

75. Zeiger, M.; Jäckel, N.; Mochalin, V. N.; Presser, V., Review: carbon onions for electrochemical energy storage. *Journal of Materials Chemistry A* **2016,** *4* (9), 3172-3196.

76. Bartelmess, J.; Giordani, S., Carbon nano-onions (multi-layer fullerenes): chemistry and applications. *Beilstein J Nanotechnol* **2014,** *5*, 1980-1998.

77. Mykhailiv, O.; Zubyk, H.; Plonska-Brzezinska, M. E., Carbon nano-onions: Unique carbon nanostructures with fascinating properties and their potential applications. *Inorganica Chimica Acta* **2017,** *468*, 49-66.

78. Jaramillo, I. C.; Gaddam, C. K.; Vander Wal, R. L.; Lighty, J. S., Effect of nanostructure, oxidative pressure and extent of oxidation on model carbon reactivity. *Combust. Flame* **2015,** *162* (5), 1848-1856.

79. de Heer, W. A.; Ugarte, D., Carbon onions produced by heat treatment of carbon soot and their relation to the 217.5 nm interstellar absorption feature. *Chemical Physics Letters* **1993,** *207* (4), 480-486.

80. Banhart, F.; Füller, T.; Redlich, P.; Ajayan, P. M., The formation, annealing and self-compression of carbon onions under electron irradiation. *Chem. Phys. Lett.* **1997,** *269* (3), 349-355.

81. Tomita, S.; Sakurai, T.; Ohta, H.; Fujii, M.; Hayashi, S., Structure and electronic properties of carbon onions. *The Journal of Chemical Physics* **2001,** *114* (17), 7477-7482.

82. Kuznetsov, V. L.; Chuvilin, A. L.; Butenko, Y. V.; Mal'kov, I. Y.; Titov, V. M., Onion-like carbon from ultra-disperse diamond. *Chemical Physics Letters* **1994,** *222* (4), 343-348.

83. Bogdanov, K.; Fedorov, A.; Osipov, V.; Enoki, T.; Takai, K.; Hayashi, T.; Ermakov, V.; Moshkalev, S.; Baranov, A., Annealing-induced structural changes of carbon onions: High-resolution transmission electron microscopy and Raman studies. *Carbon* **2014,** *73*, 78-86.

O_2-Oxidation of Individual Graphite and Graphene Nanoparticles in the 1200 – 2200 K Range: Particle-to-Particle Variations and the Evolution of the Reaction Rates and Optical Properties

Daniel J. Rodriguez, Chris Y. Lau, Bryan A. Long, Susanna An Tang, Abigail M. Friese, and Scott L. Anderson[*]

Department of Chemistry, University of Utah, 315 S. 1400 E., Salt Lake City, UT 84112

Corresponding author: anderson@chem.utah.edu

Supporting Information

Typical Raw Data

Figs. S1 and **S2** show examples of the raw data for an experiment – in this case the first part of the experiment presented in **Fig. 1** of the main text. **Fig. S1** shows measurements vs. time of the axial secular frequency, F_z, including charge stepping used to determine Q. Also shown are the mass, M, extracted from F_z, and T_{NP}, extracted from spectra like those shown in **Fig. S2**.

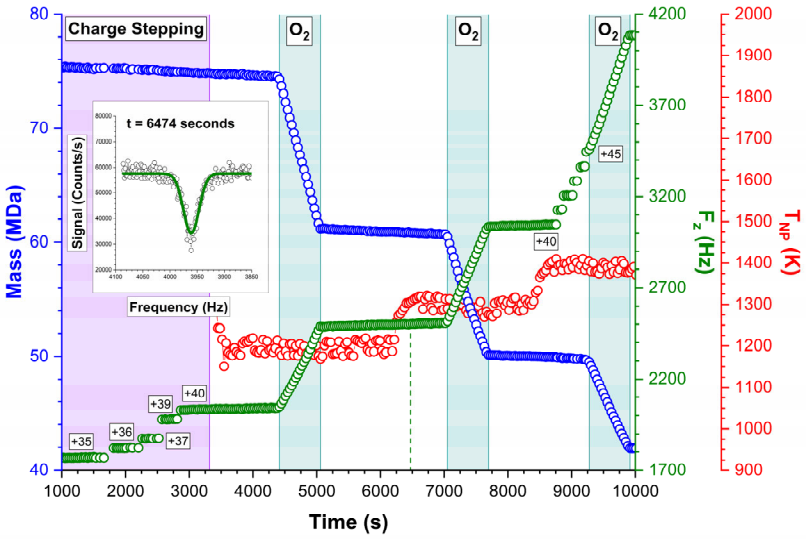

Figure S1: The early part of the experiment presented in **Fig. 1** is shown to illustrate measurement of the axial secular frequency (F_z) and charge (Q). A typical resonance scan used to determine F_z is shown in the inset. Charge steps induced by the vacuum UV lamp are shown in the time range below 3000 seconds and additional thermionic emission charge steps are visible when T_{NP} was increased from 1300 K to 1400 K.

The inset shows an example of a resonance scan used to determine F_z. The resonance scan is done by sweeping the frequency of a weak AC drive potential applied to an electrode just outside the trap. When F_{drive} is resonant with F_z, the amplitude of the NP axial motion increases enough to reduce the collection efficiency of light emitted by the NP, detected by an APD that monitors light emission from the central ~50 μm volume of the trap. As F_{drive} sweeps beyond F_z, the argon present in the trap at 2.0 mTorr pressure damps the NP motion, restoring the APD signal level. The resulting peak is then fit with a Gaussian function to extract F_z. One such scan, taking 30

seconds, was used to measure each of the F_z points in the figure. This particular scan was taken at ~6475 seconds, indicated by the green dashed vertical line in the main figure.

During the time between 1000 and 3000 seconds (purple shaded background), a vacuum UV lamp was used to drive charge steps, including one double step, taking the NP charge from +35 e to +40 e. Fitting the series of steps leads to determination of the absolute charge state Q, and once Q is known, then M can be determined from the F_z measurements via **Eqn. 1** of the main paper.

In the period between 3300 and 10000 seconds, T_{NP} was stepped from 1200 K to 1400 K while the NP was alternatively trapped in argon (unshaded background) and argon with 4.3 x 10^{-5} Torr of O_2 added (cyan shaded background). As described in the main text, by fitting the slopes of M vs. time as the NP is trapped in Ar or Ar+O_2, it is possible to derive the baseline and oxidative mass loss rates. **Fig. 1** in the main text shows the continuation of the experiment through three stepped heat ramps. Typical emission spectra and fits used to extract T_{NP} are discussed below.

It can be seen that when T_{NP} was initially raised to 1400 K, five additional charge steps occurred, taking the charge to +45 e. These steps are due to thermionic emission from the hot NP, and are often seen when NPs are initially heated to high T_{NP}. Because the F_z changes from charge steps are quantized, and typically much larger than the F_z changes due to mass loss, charge steps are easily recognized and taken into account in calculating M from the F_z measurements. Occasionally, if mass loss is very fast (or the NP fragments) there may be some ambiguity about Q. In that case, T_{NP} is lowered to ~1200 K, and the vacuum UV lamp is used to drive additional charge steps to establish the new value of Q.

T_{NP} determination

The optical system and calibration method used to obtain intensity-corrected spectra across the visible and near IR are discussed elsewhere.[1-2] Spectra are measured simultaneous with each resonance scan, thus mass and T_{NP} are determined together every ~30 seconds during the experiments. **Fig. S2** shows several typical spectra (data points) at three different temperatures, in this case for a single graphene NP undergoing an oxidation kinetic experiment. Also shown are fits to the spectra (solid curves), using the thermal emission model function given as **Eqn. 2** in the main text. The mass of the NP at the time the spectra were measured, and the values of the T_{NP} and n parameters extracted from the fits are shown in the legends. As expected, the intensity increased with T_{NP}. In addition, the emissivity parameter, n, is typically found to decrease with increasing T_{NP}.[2] During the experiment, the spectra are fit on the fly, allowing the extracted value of T_{NP} to be used in a feed-forward algorithm to control the heating laser, thus setting and stabilizing T_{NP}.

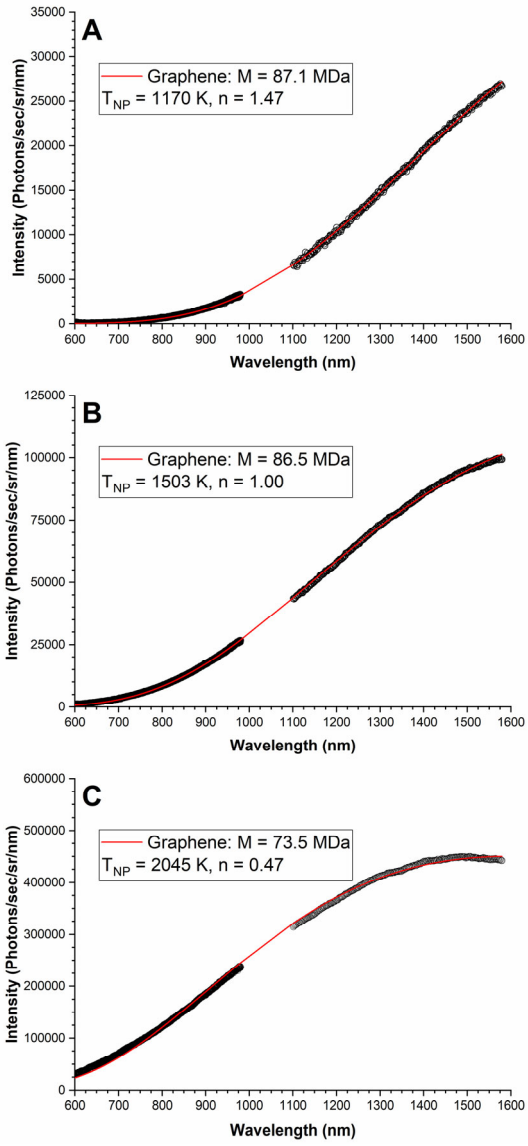

Figure S2: Example single NP emission spectra, showing fits using the thermal emission model discussed in the main text. Extracted T_{NP} and n parameters are shown in the legends.

Additional examples of Graphene T_{NP} ramp experiments

A 45.0 MDa graphene NP was subjected to a single heat ramp from 1200 K to 1700 K (**Fig. S3A**). T_{NP} was ramped in 100 K steps, and at each step the mass loss was measured with just argon in the trap, with 4.3 x 10^{-5} Torr O_2 added, then again with just argon. The baseline mass loss in argon, R_{base}, and the oxidative mass loss rate, R_{oxid}, are plotted vs. T_{NP} in **Fig. S3B** (note different scales). In this T_{NP} range, R_{base} is almost entirely due to reactions with background gas contaminants, most likely O_2.

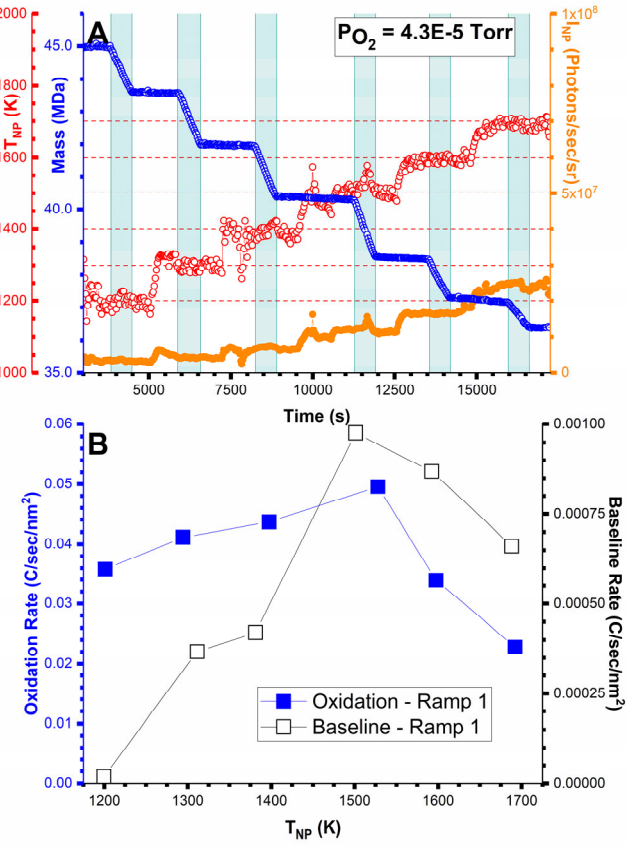

Figure S3: A). A graphene NP is T_{NP} stepped from 1200 K to 1700 K, measuring the mass and emission intensity vs. time. B). R_{oxid} and R_{base} are shown as function of T_{NP}.

In this experiment R_{oxid} increased slowly with increasing T_{NP}, peaking near 1530 K at 0.05 C/sec/nm^2, then fell rapidly at higher T_{NP}. R_{base} also peaked near 1500 K, but was ~50 times lower than R_{oxid}. Note that the oxidative mass loss was quite linear with time in each oxidation period, *i.e.*, there was no significant evolution of the NP during any given oxidation period.

Fig. S4A shows results for a 37.6 MDa initial mass graphene NP with T_{NP} ramped from 1200 K to 2000 K. T_{NP} was ramped in 100 K steps, with mass loss measured in argon, in argon with 4.3 x 10^{-5} Torr of O_2 added, then again in argon. T_{NP} was less stable in this experiment due to problems with the heating laser. When we attempted to step T_{NP} from 1600 K to 1700 K, T_{NP} became quite unstable, fluctuating between 1500 K and 1900 K requiring additional charge steps to re-establish the charge. This period, between 13700 and 18860 seconds is omitted from the figure (note break in time axis). After re-stabilizing T_{NP}, the heat ramp was continued to 2000 K, but significant T_{NP} fluctuations continued.

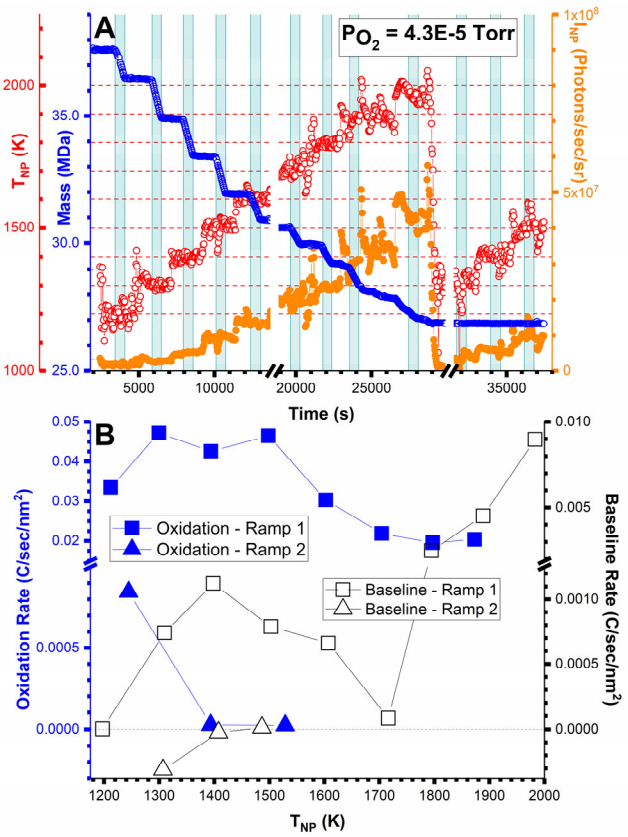

Figure S4: A). A 37.6 MDa graphene NP was studied at T_{NP} from 1200 K to 2000 K, measuring the mass vs. time in argon and O_2 at each T_{NP}. The NP was cooled to T_{NP} = 1300 K, then a 2nd ramp from T_{NP} = 1300 K to 1500 K was run. I_{NP} is also shown. B). The T_{NP} dependence for R_{oxid} and R_{base} is shown for each T_{NP} ramp.

T_{NP} was then dropped to start a 2nd heat ramp, however, between ~29900 and 31500 seconds, the laser again became unstable, and this time range is also omitted. The 2nd heat ramp was eventually abandoned at ~1500 K due to continued problems with laser stabilization (and a new laser was used in subsequent experiments).

The R_{oxid} and R_{base} rates are plotted versus T_{NP} in **Fig. S4B**. Note that for the higher end of this T_{NP} range, sublimation becomes fast and dominates R_{base} (note break in right hand axis). The oxidation rate during the 1st heat ramp was broadly peaked in the 1300 – 1500 K range, then dropped at higher T_{NP}.

Note that the laser became increasingly unstable as the first heat ramp progressed, therefore the ramp was terminated after the 2000 K T_{NP} step, and the temperature was dropped back to 1300 K but continued to fluctuate. We attempted a 2nd heat ramp, however, because the laser continued to be very unstable, the ramp was terminated at 1500 K.

Even with the laser instability problems, this experiment provides some useful insight. "Normal" baseline and oxidative mass loss rates were observed during the 1st heat ramp, resulting in useable R_{oxid} values, as shown in **Fig. S4B**. Additionally, this experiment provides a good example of how drastically the reactivity properties of an NP can change during an experiment.

Second ramp of the experiment in Fig. 2, main text

The 2nd T_{NP} ramp for the graphite NP experiment presented in **Fig. 2** of the main text is shown in **Fig. S5A**. As in **Fig. 2**, each T_{NP} step was ~30 minutes, with the baseline rate of mass loss with the NP trapped in Ar measured for the first and final ~10 minutes, and with a ~10 minute oxidation period in the middle of each T_{NP} step. P_{O2} was 2.1 x 10^{-5} Torr during each oxidation period.

A zoomed in view of the low T_{NP} region from 1600 K to 1800 K is given in **Fig. S5B**, and comparison with **Fig. 2B** clearly shows the dramatic slowing of both the baseline and oxidative mass loss rates in the 2nd heat ramp. **Fig. S5C** shows a zoomed in view of the high T_{NP} range from 2000 K to 2300 K, where the baseline rate is almost entirely attributable to sublimation. Note that the slope of mass vs. time hardly changed when O_2 was added, demonstrating that $R_{oxid} << R_{base}$

(*i.e.*, $R_{sublimation}$) in this T_{NP} range. Note also that each time T_{NP} was raised, the initial sublimation rate was high, but slowed perceptibly after few minutes. Similar slowing of the sublimation rate was noticeable, but much less dramatic in the 1st heat ramp (**Fig. 2C**).

In **Fig. S5D**, R_{oxid} and R_{base} are plotted versus T_{NP}. The axis (right hand) for R_{base} has a break in order to more clearly show the dramatic increase in sublimation rate with T_{NP}. R_{oxid} is near zero in the 2nd ramp below 1800 K, peaks at ~2000 K, then decreases to zero again by 2200 K, within the experimental uncertainty. The uncertainty in R_{oxid} at high T_{NP} is large because R_{base} is very large compared to R_{oxid}, resulting in large uncertainty in the subtraction needed to extract R_{oxid} from the total mass loss rates.

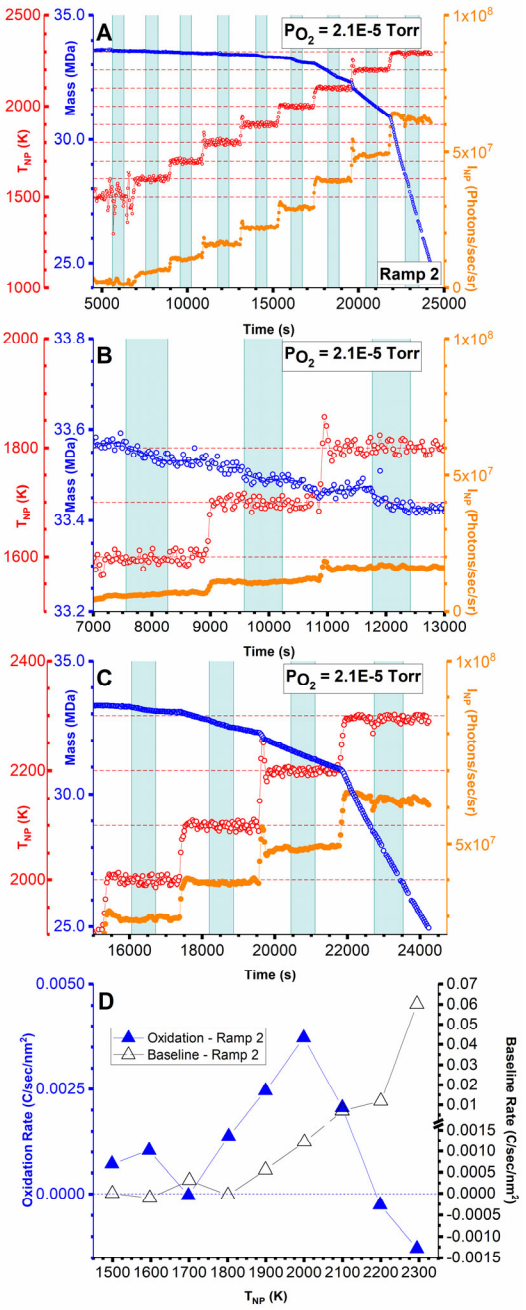

Figure S5: A). The second heat ramp for the NP examined in **Fig. 2** of the main text is shown. B). A magnified view of the region from T_{NP} = 1600 K to 1800 K. C). Magnified view for T_{NP} = 2000 K to 2300 K. D). R_{oxid} and R_{base} are plotted versus T_{NP}.

Another graphite NP T_{NP}-ramping experiment

A 23.2 MDa graphite NP was charge stepped at low T_{NP} (not shown) then subjected to two stepwise heat ramps, alternately measuring sublimation and oxidation during each T_{NP} step. The first ramp, shown in **Fig. S6A**, ran from 1700 K to 2100 K, then the NP was cooled to 1500 K and ramped again to 2100 K. During the 1st heat ramp, R_{base} showed a fast increase with increasing T_{NP}, as expected because sublimation should become fast in this T_{NP} range. The maximum value of R_{oxid} in the 1st heat ramp was at low T_{NP}, declining with increasing T_{NP}. The maximum value of R_{oxid} during the 1st heat ramp was only 3.2 x 10^{-3} C/sec/nm^2 – considerably lower than the peak rates in the other experiments. This, at least partly, reflects the use of a lower O_2 pressure in this experiment (2.1 x 10^{-5} Torr).

The sublimation behavior in the 2nd heat ramp (**Fig. S6B**) was also typical – R_{base} increasing with increasing T_{NP} but significantly lower than R_{base} in the 1st ramp, as seen for all the NPs. The oxidation behavior was, however, quite anomalous. During

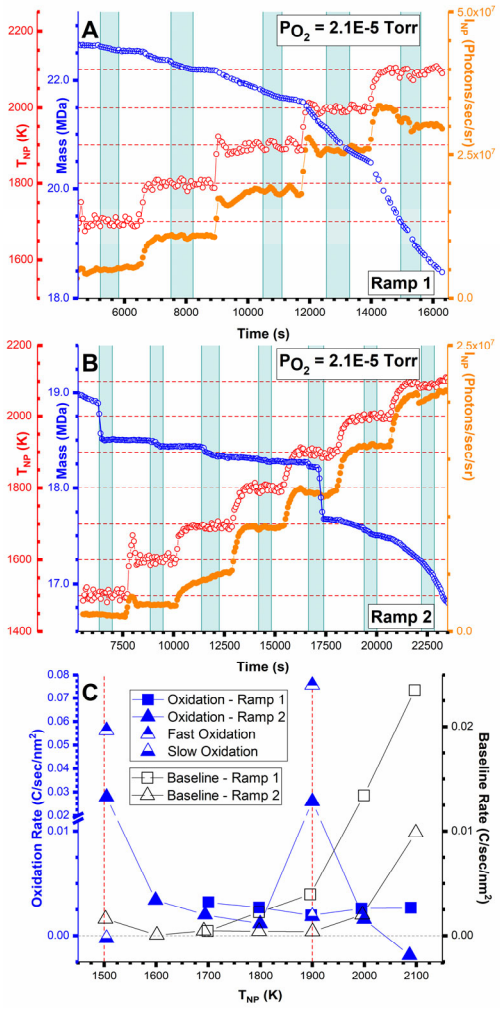

Figure S6: A). A ~23.2 MDa graphite NP is T_{NP} stepped from 1500 to 2100 K, while mass vs. time is measured in both Ar and Ar with added O_2. I_{NP} is also shown. B). Mass vs. time during a 2nd T_{NP} ramp. Note brief periods of very fast mass loss at T_{NP} = 1500 K and 1900 K. C). R_{oxid} and R_{base} are plotted as a function of T_{NP}. For 1500 and 1900 K, where two distinct rates were observed, partially filled symbols are used to indicate the two rates.

most of the oxidation periods, R_{oxid} was similar to the values seen in the first heat ramp, but during the oxidation periods at 1500 K and 1900 K, the mass loss rates were wildly variable. When O_2 was first added at 1500 K, there was immediate very fast loss of ~0.4 MDa (2% of the mass at that time), but then the mass loss rate slowed to near zero and remained low for the rest of that oxidation period. Note also that the baseline mass loss rate after this oxidation period was also near zero, and much slower than the rate observed just before the fast mass loss event. Then, during the 1600, 1700, and 1800 K steps, behavior was "normal", *i.e.*, the NP showed sublimation increasing with T_{NP}, and R_{oxid} was relatively steady, and slowly decreased with T_{NP}, similar to behavior seen for the other graphitic NPs. Then, when O_2 was added at 1900 K, the initial mass loss rate was slow, but then after a few minutes the rate suddenly increase, such that ~0.5 MDa was lost in a few minutes. To test whether this fast mass loss was due to oxidation or sublimation, the O_2 was shut off after a few minutes, and the fast mass loss stopped immediately. Finally, the behavior during the 2000 and 2100 K T_{NP} steps reverted to "normal", *i.e.*, sublimation increasing with T_{NP} and little effect of adding O_2.

To show the large variations in R_{oxid} at 1500 and 1900 K, **Fig. S6C** shows both the fast and slow rates as half-filled triangles, and the average R_{oxid} as solid triangles.

Another example of long time, constant T_{NP}, constant P_{O2} oxidation rate evolution

Fig. S7 shows a constant T_{NP}, constant P_{O2} experiment on a 32.6 MDa graphite NP heated to 1700 K, and exposed to O_2 at a partial pressure of 2.1 x 10^{-5} Torr. Roman numerals indicate time periods with near-constant mass loss rates, from which values of R_{base} and R_{oxid} were extracted by linear fits. Those rates are given in the box in the figure. As in the other constant T_{NP}, constant P_{O2} experiments, the oxidation rates varied non-monotonically with time, by over a factor of 20. Note, however, that unlike the previous examples, where the NPs became nearly inert at long

times, here the rates generally slowed with time, but not drastically. The final oxidation rate was only ~8 times slower than the initial rate, although it is possible that if the experiment had continued longer, further slowing would have occurred.

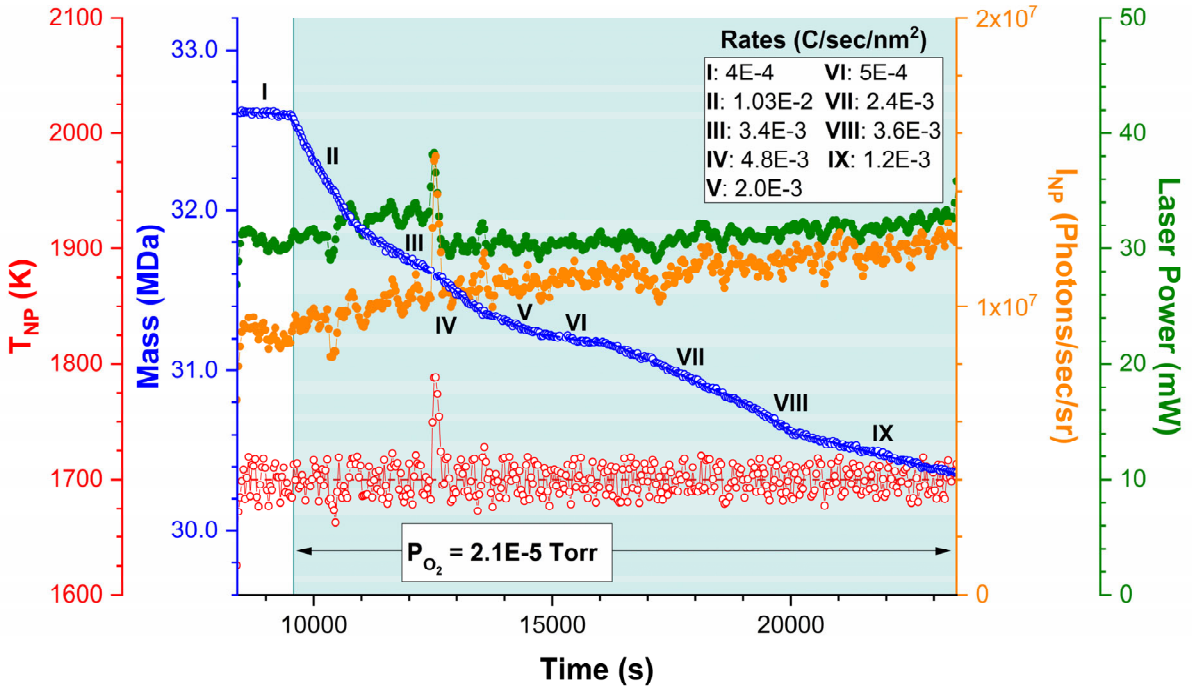

Figure S7: A 32.6 MDa graphite NP is held at T_{NP} = 1700 K and P_{O2} = 2.1 x 10^{-5} Torr. I_{NP} is seen to increase as the NP loses mass. R_{base} is measured before the start of oxidation, and the baseline-corrected R_{oxid} values are observed to vary non-monotonically with time by factors of up to ~20.

This figure also shows interesting evolution of the NP optical properties. Note that I_{NP} increased monotonically by ~30% over the course of the experiment, *i.e.*, the NP got brighter at constant T_{NP}, even as it got smaller. If the emission is corrected for the ~7% decrease in NP mass/volume,[2] the emissivity is seen to increase by nearly 40%. The fact that the emission brightened by ~30% implies a significant increase in radiative cooling power. It is, thus, interesting that the laser power required to heat the NP to 1700 K only increased by ~2% over the

experiment. This implies that the absorption cross section for the 532 nm heating laser also increased by ~30% during the experiment, such that laser heating and radiative cooling remained in balance.

Another pre-heating experiment.

Fig. 6 in the main text shows a simple experiment, in which a graphite NP was pre-heated at 1900 K, then oxidized at 1700 K, with the result that the 1700 K oxidation rate was substantially faster than that for any of the other graphite NPs. **Fig. S8** shows a more elaborate experiment of this type.

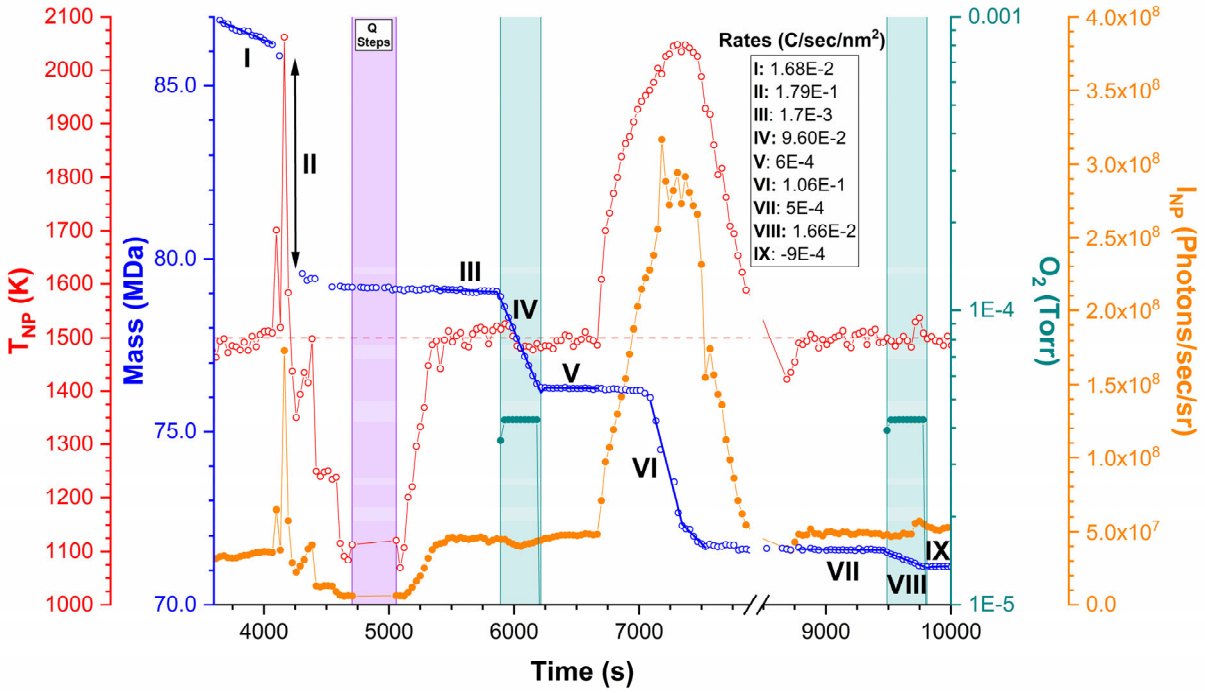

Figure S8: An 86.9 MDa graphene NP is flashed to T_{NP} = ~2050 K before being oxidized at T_{NP} = 1500 K. The NP was then annealed at >1950 K followed by oxidation at 1500 K giving a ~5 times slower rate.

An 86.9 MDa graphene nanoplatelet was initially trapped in 2.0 mTorr of Ar at 1500 K to establish an initial baseline mass loss rate of ~1.68 x 10^{-2} C/sec/nm^2, attributed to a combination of sublimation and background reactions (time period I). The NP was then briefly flashed to T_{NP}

> 2050 K (II) during which time it lost 6.3 MDa. Note that during such fast mass loss, it is impossible to rule out fragmentation of the NP which sometimes changes the charge, therefore, T_{NP} was lowered to ~1100 K for charge stepping to re-establish the charge and mass. The NP was then heated to 1500 K, to re-measure the baseline mass loss rate (III), which was found to be ten times slower than the initial baseline rate. Next, O_2 was added at $P_{O2} = 4.3 \times 10^{-5}$ Torr, resulting in an oxidative mass loss rate (IV) corresponding to $R_{oxid} = 9.60 \times 10^{-2}$ C/sec/nm^2, etching away ~3 MDa. This rate is faster than those of all but one of the NPs at 1500 K summarized in **Fig. 9**. When the O_2 flow was stopped (V), the baseline rate had dropped by another factor of ~3 to just 6×10^{-4} C/sec/nm^2. Thus, in this case, we can say that the initial brief high T_{NP} period resulted in a substantial drop in the baseline rate, with a further decrease after oxidation, however, the oxidation rate was still quite fast.

In the second half of the experiment, the NP was further annealed by ramping T_{NP} to ~2050 K, but this time holding T_{NP} above 1950 K for six minutes, resulting in loss of another 4.2 MDa with a sublimation rate, $R_{base} = 1.06 \times 10^{-1}$ C/sec/nm^2 (VI). The ~10 minute break in the time axis represents a period when the data acquisition software had to be reinitialized due to a camera failure, during which time T_{NP} was held at ~1400 K. Then a final cycle of measuring the baseline rate (VII), oxidation (VIII), and then re-measuring the baseline rate (IX) was carried out. Note that the oxidation rate was more than an order of magnitude slower after the second, longer high T_{NP} heating period (VIII, 1.66×10^{-2} C/sec/nm^2) than it was after the initial fast high T_{NP} flash (IV, 9.60×10^{-2} C/sec/nm^2).

A P_{O2} ramping experiment on a graphene NP

Fig. 7 introduced a P_{O2} ramping experiment, for a graphite NP at 1900 K. **Fig. S9** summarizes a similar experiment for a 73.0 MDa graphene NP, also carried out at T_{NP} = 1900 K. P_{O2} was ramped twice in stepwise fashion from 2.1 x 10^{-5} Torr to 8.5 x 10^{-5} Torr, with ~11 MDa and 7.5 MDa mass loss, respectively, during the two P_{O2} ramps, mostly during the oxidation periods. Between the two P_{O2} ramps, the NP was annealed to T_{NP} > 2100 K for 7.5 minutes, losing an additional 2.4 MDa due to sublimation. The R_{oxid} values measured at each P_{O2} for both P_{O2} ramps are plotted in **Fig. S9B**, as are the averaged R_{base} values measured before and after each oxidation period. I_{NP} is also plotted and apart from the expected increase during the annealing period, only a modest decrease is observed, as might be expected from the loss in NP volume during the experiment. The sharp deviations in I_{NP} and T_{NP} are due to instabilities of the heating laser.

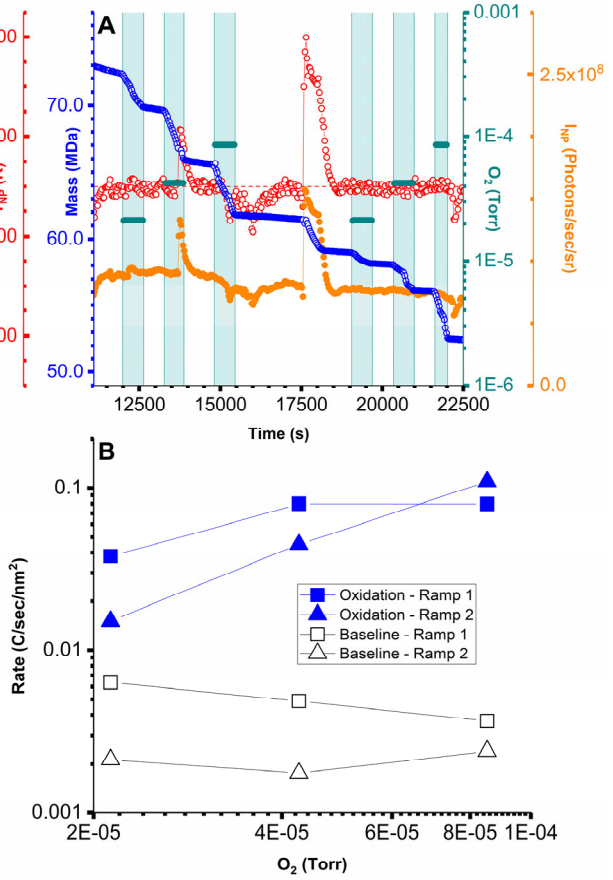

Figure S9: A). A 73.0 MDa graphene NP is heated to T_{NP} = 1900 K. Then P_{O2} is ramped from 2.1 x 10^{-5} to 8.5 x 10^{-5} Torr. Two P_{O2} ramps are shown with 7.5 minutes of annealing between them at T_{NP} = 2100 K. B). R_{oxid} and R_{base} are plotted for the two P_{O2} ramps.

The R_{oxid} values in both heat ramps were observed to increase with increasing P_{O2}, and while the P_{O2} dependence for this NP is weaker and less complicated than for the graphite NP in **Fig. 7**, it is also clear that R_{oxid} is not simply linear in P_{O2}. There was a modest decrease in R_{oxid} after the high T_{NP} annealing period, but at high P_{O2}, R_{oxid} was higher in 2nd ramp than the 1st. The mass rates during the oxidation periods were generally constant, however, during the two final oxidation periods, after 20000 seconds, the rates oscillated, similar to the oscillations for the graphite NP shown in the inset to in **Fig. 7**.

Summary of oxidation efficiencies seen in 2nd and 3rd T_{NP} ramps and 2nd P_{O2} ramps

Fig. S10 presents all the oxidation efficiencies measured in later parts of the experiments that are summarized in **Fig. 9** of the main text. Comparison of **Fig. S10** and **Fig. 9** shows the dramatic reduction in oxidation efficiencies seen over time.

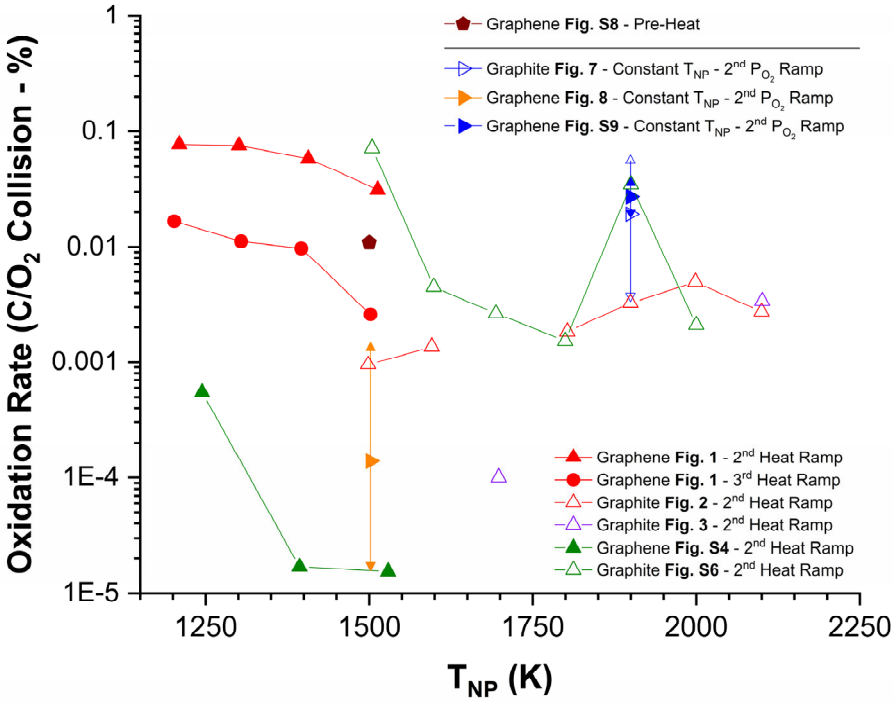

Figure S10: Summary of oxidation efficiencies observed during 2nd and 3rd T_{NP} ramps and 2nd P_{O2} ramps on the indicated NPs. The format is the same as in **Fig. 9** in the main text.

REFERENCES

1. Long, B. A.; Rodriguez, D. J.; Lau, C. Y.; Anderson, S. L., Thermal emission spectroscopy for single nanoparticle temperature measurement: optical system design and calibration. *Appl. Opt.* **2019,** *58* (3), 642-649.

2. Long, B. A.; Rodriguez, D. J.; Lau, C. Y.; Schultz, M.; Anderson, S. L., Thermal Emission Spectroscopy of Single, Isolated Carbon Nanoparticles: Effects of Particle Size, Material, Charge, Excitation Wavelength, and Thermal History. *J. Phys. Chem. C* **2020,** *124*, 1704-1716.

A

Time (s)	Mass (Da)	Mass (Da) - Reg	Time (s)	T_{NP} (K)	I_{NP} (Photons/sec/sr)
3515	74763099		3515	1215.495	3165267.013
3547	74769669		3547	1150.514	2894322.35
3579	74707938	74776238.8	3579	1206.456	2800591.474
3611	74766441	74767190.65	3611	1183.606	2848841.472
3643	74791964	74758142.49	3644	1179.127	2895122.132
3675	74732516	74749094.34	3676	1176.831	2991113.8
3708	74766971	74739763.43	3708	1194.892	3085252.086
3740	74742930	74730715.28	3740	1184.953	3116357.054
3772	74694782	74721667.12	3772	1180.394	3203761.411
3804	74747570	74712618.97	3804	1177.361	3317923.304
3836	74799373	74703570.81	3836	1205.246	3385123.082
3868	74705398	74694522.66	3869	1211.122	3441183.887
3901	74626037	74685191.75	3901	1207.948	3375337.808
3933	74713784	74676143.6	3933	1210.298	3341474.423
3964	74619975	74667378.2	3965	1217.373	3371374.984
3998	74681916	74657764.53	3998	1218.724	3264286.287
4029	74618383	74648999.14	4030	1188.909	3135254.761
4062	74668265	74639668.23	4062	1184.735	3045701.176
4093	74576100	74630902.83	4094	1183.718	3054519.994
4126	74580265	74621571.92	4126	1189.302	3186638.692
4158	74652773	74612523.76	4158	1214.807	3367721.909
4190	74532070	74603475.61	4190	1181.772	3316385.392
4223	74651277	74594144.7	4223	1211.033	3296252.616
4254	74626557	74585379.3	4255	1190.174	3337756.639
4286	74511100	74576331.15	4287	1191.971	3271539.21
4319	74565117	74567000.24	4319	1184.553	3291712.614
4351	74595251	74557952.08	4351	1194.538	3317862.427
4383	74552103	74548903.93	4383	1213.113	3461423.132
4415	74295945	74209183.16	4416	1185.206	3437952.286
4446	73686469	73582518.31	4448	1177.628	3364765.869
4479	73031652	72915423.46	4480	1205.547	3497784.379
4511	72291248	72268543.61	4512	1186.737	3539403.804
4544	71603881	71601448.77	4544	1176.719	3460617.956
4576	70912262	70954568.92	4576	1203.429	3621935.902
4608	70303725	70307689.07	4609	1204.856	3529042.868
4640	69592324	69660809.22	4641	1178.076	3455606.695
4673	68922863	68993714.37	4673	1199.855	3428472.765
4705	68328923	68346834.52	4705	1176.498	3484414.41
4737	67663942	67699954.68	4737	1204.477	3548160.412
4769	67021501	67053074.83	4769	1186.13	3524779.477
4801	66386154	66406194.98	4802	1199.391	3534191.246
4833	65764350	65759315.13	4834	1181.962	3586741.578
4865	65058378	65112435.28	4866	1177.295	3624277.2
4898	64383493	64445340.43	4898	1180.677	3753122.201
4930	63687093	63798460.58	4930	1201.731	3771732.092
4962	62979717	63151580.73	4963	1177.96	3793632.217
4995	62330530	62484485.89	4995	1200.938	3814741.169
5026	61669242	61857821.03	5027	1176.366	3807418.265
5059	61187796	61190726.19	5059	1168.504	3733471.835
5093	61202052	60503416.35	5091	1175.23	3831029.093
5123	61224014	61184720.61	5123	1200.718	4077317.911
5155	61189811	61175856.98	5155	1210.102	4176927.045
5187	61150969	61166993.35	5188	1208.563	4124645.409
5220	61142824	61157852.74	5220	1208.474	4017593.984
5252	61179975	61148989.11	5252	1180.019	3942259.626
5283	61117645	61140402.47	5284	1181.191	3834809.029
5316	61131507	61131261.86	5316	1182.242	3951310.468
5348	61109084	61122398.23	5348	1210.189	4117321.199
5380	61097032	61113534.6	5381	1187.851	4132900.637
5412	61095330	61104670.97	5413	1175.457	4039986.239
5445	61119936	61095530.36	5445	1203.743	4082275.166
5476	61090190	61086943.72	5477	1208.912	4215732.348
5509	61065218	61077803.1	5509	1183.467	4110786.584
5541	61072539	61068939.47	5542	1176.524	4097130.885
5573	61075995	61060075.84	5574	1175.826	4198592.412
5605	61026827	61051212.22	5606	1214.695	4397060.535
5638	61059125	61042071.6	5638	1211.571	4379384.026
5670	61057761	61033207.97	5670	1209.427	4277900.988
5702	61013010	61024344.35	5702	1205.798	4132092.663
5735	61023630	61015203.73	5735	1214.363	4136567.998
5766	61005645	61006617.09	5767	1218.449	4062259.197
5798	60956815	60997753.46	5799	1190.786	3916555.414
5831	61013183	60988612.85	5831	1185.926	3863925.456
5862	60938358	60980026.21	5863	1205.125	3920434.427
5896	60960940	60970608.6	5896	1186.4	3974152.536
5927	60986659	60962021.96	5928	1211.775	3964014.132
5959	60924994	60953158.33	5960	1213.515	4013852.454
5992	60920094	60944017.72	5992	1211.915	3959753.468
6024	60908211	60935154.09	6024	1188.159	3864931.803
6056	60929863	60926290.46	6056	1180.124	3733625.594
6088	60908757	60917426.84	6088	1184.444	3785826.271
6120	60918685	60908563.21	6121	1216.313	4054832.49
6152	60918816	60899699.58	6153	1213.572	4168461.998
6185	60925546	60890558.96	6185	1187.099	4086496.424
6217	60905231	60881695.34	6217	1214.905	4567619.788
6249	60895843		6249	1257.07	5687581.332
6281	60893003		6282	1272.976	6228077.376
6313	60868204		6314	1277.649	6413196.582
6346	60868243	60868679.78	6346	1285.168	6644131.673
6378	60832534	60860393.06	6378	1292.326	6694447.285
6410	60861009	60852106.34	6410	1302.988	6858276.501
6442	60889198	60843819.62	6443	1303.162	6722071.848
6474	60833655	60835532.9	6475	1306.189	6686743.467
6507	60816992	60826987.22	6507	1309.698	6692154.078
6539	60830850	60818700.5	6539	1313.643	6602998.446
6571	60804833	60810413.79	6571	1314.37	6461996.413
6603	60774802	60802127.07	6603	1318.559	6366831.287
6635	60791598	60793840.35	6636	1318.24	6269388.958
6667	60782210	60785553.63	6668	1288.849	5994648.523
6700	60762907	60777007.95	6700	1312.413	5889299.169
6732	60745288	60768721.23	6732	1320.65	6073147.143
6764	60781309	60760434.51	6764	1318.176	5919243.766
6796	60809771	60752147.79	6796	1292.69	5819808.198
6828	60742148	60743861.07	6828	1285.103	5638304.14
6861	60717180	60735315.4	6861	1315.429	5729207.835
6893	60716342	60727028.68	6893	1318.905	5801689.275
6925	60743606	60718741.96	6925	1315.961	5714404.295
6956	60682335	60710714.2	6957	1286.118	5481983.925
6989	60696293	60702168.52	6989	1288.065	5437480.999
7021	60705073	60693881.8	7021	1312.85	5504405.892
7052	60479193	60219179.99	7054	1289.838	5642938.027
7083	59886366	59708163.19	7086	1312.813	5531320.386
7117	59279856	59147693.14	7118	1282.736	5531101.392
7150	58684579	58603707.51	7150	1293.12	5405593.554
7182	58055768	58076206.29	7182	1294.047	5409179.184
7214	57465664	57548705.07	7214	1307.303	5440876.431
7246	56847611	57021203.85	7247	1297.381	5466750.91
7279	56321285	56477218.22	7279	1299.444	5377240.679
7311	55819953	55949717	7311	1311.753	5410876.928
7342	55273015	55438700.2	7343	1285.803	5221536.699
7375	54769954	54894714.56	7375	1277.446	5144502.036
7407	54243013	54367213.35	7407	1287.686	5135259.225
7439	53721835	53839712.13	7440	1293.896	5143502.104
7472	53230180	53295726.5	7472	1279.012	5169144.195
7504	52749703	52768225.28	7504	1272.967	5239915.53
7535	52220754	52257208.47	7536	1296.63	5202604.161
7568	51763127	51713222.84	7568	1306.031	5328380.873
7600	51291738	51185721.62	7600	1279.6	5277431.023
7632	50833881	50658220.4	7632	1269.494	5029610.578
7664	50363703	50130719.18	7665	1282.539	5188615.678
7698	50129694	50109075.87	7697	1274.981	5225329.483
7730	50104126	50104389.55	7729	1274.118	5437647.805
7761	50109518	50099849.68	7761	1270.585	5596279.693
7793	50104254	50095163.36	7793	1302.823	5795871.252
7825	50098130	50090477.04	7825	1278.232	5926896.106
7857	50108377	50085790.72	7858	1306.961	5984915.457
7889	50061946	50081104.4	7890	1305.58	5983317.739
7922	50045105	50076271.63	7922	1309.565	5954005.523
7954	50057369	50071585.31	7954	1297.454	5787337.683
7986	50066242	50066898.99	7986	1305.508	5741286.711
8018	50056464	50062212.67	8018	1286.25	5762745.946
8050	50036926	50057526.35	8050	1303.691	5641275.561
8083	50042977	50052693.59	8083	1314.185	5770276.254
8114	50061937	50048153.71	8115	1316.409	5725294.377
8146	50024563	50043467.4	8147	1288.374	5554833.131
8179	50034819	50038634.63	8179	1284.226	5481560.851
8211	50030543	50033948.31	8211	1300.993	5569654.143
8243	50034719	50029261.99	8243	1286.295	5599636.045
8275	50025747	50024575.67	8276	1310.467	5688111.794
8307	50029881	50019889.35	8308	1301.932	5763657.158
8340	50040626	50015056.58	8340	1306.387	5666946.478
8371	50010996	50010516.71	8372	1299.405	6132419.146
8404	50007267	50005683.94	8404	1307.538	6673549.221
8436	50007056		8436	1327.601	7723266.49
8468	49997800		8468	1333.183	8367198.459
8500	50000900		8501	1365.686	8889412.852
8532	49980514	49996654.35	8533	1373.922	9487719.978
8564	49965634	49984511.63	8565	1377.653	9678225.586
8596	49936185	49972368.92	8597	1382.718	10003700
8629	49959836	49959846.75	8629	1394.542	10209800
8661	49959290	49947704.04	8661	1400.155	10206500
8693	49940391	49935561.33	8693	1403.016	10287900
8725	49954702	49923418.61	8726	1379.144	10321900
8757	49940867	49911275.9	8758	1409.755	10371800
8780	49905741	49902548.33	8790	1393.97	10545700
8828	49916424	49884334.26	8822	1395.803	10369800
8853	49827621	49874847.76	8854	1383.303	10713300
8878	49859618	49865361.27	8886	1398.541	10501300
8924	49833103	49847906.12	8919	1396.908	10546800
8951	49860183	49837660.71	8951	1384.93	10501500
8982	49850726	49825897.46	8983	1405.273	10485200
9015	49828007	49813375.28	9015	1389.841	10514200
9038	49803568	49804647.71	9047	1409.097	10650400
9085	49787483	49786813.1	9079	1401.235	10709500
9111			9112	1385.879	11112700
9140	49802723	49765942.81	9144	1394.394	11044600
9181	49734133	49750384.96	9176	1410.085	10820200
9208	49732562	49740139.55	9208	1383.434	10747600
9230	49683680	49731791.44	9240	1393.434	10661300
9276	49509409	49492420.33	9272	1404.268	10826800
9303	49185074	49160175.35	9304	1380.372	10715500
9336	48790288	48754098.15	9337	1399.65	10665700
9368	48389595	48360326.33	9369	1378.471	10556600
9400	47986161	47966554.5	9401	1379.29	10476400
9433	47596428	47560477.3	9433	1374.033	10545200
9464	47177925	47179010.85	9465	1387.41	10507100
9497	46765362	46772933.65	9497	1400.941	10695300
9529	46351455	46379161.82	9529	1396.08	10549600
9561	45957367	45985389.99	9561	1388.956	10454600
9593	45544958	45591618.17	9594	1373.632	10316300
9625	45120485	45197846.34	9626	1393.257	10375400
9658	44729695	44791769.14	9658	1378.747	10419700
9690	44354193	44397997.31	9690	1403.722	10545200
9722	43948662	44004225.49	9722	1375.921	10516700
9754	43577339	43610453.66	9754	1384.766	10360400
9786	43223882	43216681.83	9787	1405.182	10590000
9818	42864925	42822910.01	9819	1398.145	10530200
9850	42506232	42429138.18	9851	1377.556	10098000
9882	42129118	42035366.35	9883	1377.178	9975085.055
9917	41920265	41923655.06	9915	1379.027	9988214.899
9949	41913214	41919762.47	9947	1386.109	10071400
9979	41921297	41916113.16	9979	1391.251	10244900
10011	41906903	41912220.57	10012	1371.243	10326200
10044	41919791	41908206.33	10044	1371.281	10476100
10075	41908577	41904435.38	10076	1401.209	10671100
10108	41903875	41900421.14	10108	1406.694	10888400
10140	41892617	41896528.55	10140	1408.696	10940400
10172	41878906	41892635.95	10172	1394.034	10879100
10204	41896428	41888743.36	10204	1383.645	10863000
10236	41883419	41884850.76	10237	1396.36	10904500
10268	41882759	41880958.17	10269	1416.941	11168900
10300	41888268	41877065.57	10301	1416.413	11137600
10332	41867102	41873172.98	10333	1395.24	11037600
10365	41874697	41869158.74	10365	1401.572	10844900
10397	41864797	41865266.15	10397	1390.339	10785700
10429	41843578	41861373.55	10429	1387.079	10817500
10462	41855963	41857359.31	10461	1390.582	10917000
10493	41859791	41853588.36	10494	1406.683	11001100
10525	41851484	41849695.77	10526	1381.667	11091300
10558	41852431	41845681.53	10558	1377.601	11100100
10590	41836521	41841788.94	10590	1418.749	12225300
10622	41819479		10622	1437.907	13518400
10654	41829591		10654	1447.813	14153400
10686	41832311		10686	1455.894	14772700
10718	41820292		10719	1467.267	15315100
10750	41810974		10751	1475.297	15478800
10783	41816549		10783	1482.234	15771600
10815	41819595	41827256.48	10815	1491.156	16018100
10847	41799701	41818036.38	10847	1465.119	16115000
10879	41795749	41808816.29	10879	1488.34	16116600
10911	41792560	41799596.19	10912	1492.644	16211800
10943	41789975	41790376.1	10944	1502.203	16465800
10976	41795996	41780867.88	10976	1503.933	16396700
11007	41783901	41771935.91	11008	1490.355	16276200
11040	41763830	41762427.69	11040	1509.916	16493900
11072	41770069	41753207.59	11072	1512.081	16347400
11104	41764695	41743987.5	11104	1487.022	16325700
11125	41735588	41737936.81	11137	1500.925	16257000
11174	41714603	41723818.54	11169	1502.168	16192100
11201	41718402	41716039.09	11201	1494.793	16154900
11233	41718850	41706818.99	11233	1499.056	16018300
11265	41715792	41697598.9	11265	1494.958	16005900
11286	41687285	41691548.21	11297	1504.652	16192400
11335	41682351	41677429.94	11329	1493.219	16109800
11361	41660508	41669938.62	11362	1481.406	15969200
11383	41644483	41663599.8	11394	1482.127	16364000
11431	41638237	41649769.66	11426	1493.166	16360500
11458	41640829	41641990.21	11458	1478.431	16425900
11488	41529059	41417589	11490	1499.343	16614600
11520	41269929	41186683.54	11522	1476.949	16681500
11554	41004806	40941346.48	11554	1495.345	16672800
11586	40729862	40710441.02	11587	1508.713	16810500
11618	40458694	40479535.55	11619	1502.657	16650900
11651	40204303	40241414.29	11651	1503.899	16535500
11683	39954961	40010508.82	11683	1483.151	16442900
11715	39710929	39779603.36	11715	1501.726	16461200
11747	39465039	39548697.89	11747	1505.251	16416700
11779	39243483	39317792.43	11779	1516.226	16498500
11811	39025476	39086886.96	11811	1514.829	16272600
11843	38812600	38855981.49	11844	1488.873	16086600
11875	38595290	38625076.03	11876	1488.477	15871800
11907	38372553	38394170.56	11908	1486.112	15992800
11940	38156371	38156049.3	11940	1483.847	15963300
11972	37949875	37925143.84	11972	1502.541	16083900
12003	37714888	37701454.17	12004	1473.417	15760900
12036	37494440	37463332.91	12036	1470.33	15608000
12068	37289413	37232427.44	12068	1501.414	15744100
12100	37093688	37001521.97	12101	1475.204	15959700
12134	36983896	36998227	12133	1499.643	15881000
12166	36984397	36991346.69	12165	1502.345	16041400
12196	36974851	36984896.4	12197	1478.399	16160000
12229	36980921	36977801.07	12229	1479.232	16189400
12261	36974654	36970920.76	12261	1476.317	16448400
12293	36971032	36964040.45	12293	1477.313	16525700
12325	36965263	36957160.14	12326	1500.158	16633900
12357	36959910	36950279.83	12358	1505.438	16923700
12389	36957529	36943399.52	12390	1507.188	16925200
12422	36950426	36936304.2	12422	1511.07	16978000
12454			12454	1525.639	17974800
12481	36936679	36923618.62	12486	1528.364	17663000
12523	36897180	36914588.21	12518	1518.836	16910200
12550	36898497	36908782.95	12550	1525.84	16696300
12582	36890616	36901902.64	12582	1501.316	16680500
12614	36889411	36895022.33	12614	1503.742	16404400
12646	36886138	36888142.01	12647	1527.104	16656800
12678	36881462	36881261.7	12679	1512.314	16670400
12710	36879214	36874381.39	12711	1498.877	16557200
12743	36883571		12743	1509.512	16607400
12775	36878192		12775	1520.327	16833000
12807	36881845		12807	1490.515	15771600
12839	36878637		12840	1476.476	14891700
12871	36878257		12872	1472.246	13931600
12903	36870163		12904	1450.336	12849900
12936	36869841		12936	1430.473	11684300
12968	36873999		12968	1416.328	10957800
12999	36864658		13000	1402.846	10040400
13032	36872470		13032	1380.189	8977325.423
13064	36866021		13064	1358.685	7891962.169
13096	36859478		13097	1363.013	6992132.098
13128	36857003		13129	1316.772	5988398.46
13160	36865523		13161	1293.205	5105011.209
13192	36862083		13193	1261.094	4248468.696
13225	36863897		13225	1275.71	3933461.824
13257	36866885		13257	1239.853	3523423.04
13289	36868124		13289	1224.403	3198045.106
13321	36854974		13321	1214.735	3065008.963
13353	36849306		13354	1210.483	2975516.758
13385	36850184	36855566.78	13386	1207.522	2953030.656
13417	36846603	36854457.75	13418	1201.354	2959864.787
13450	36856694	36853314.07	13450	1222.051	2948930.21
13481	36846140	36852239.69	13482	1197.582	2912423.82
13514	36843472	36851096.01	13514	1189.85	2861324.618
13546	36853749	36849986.98	13546	1189.164	2842159.693
13578	36850263	36848877.95	13578	1192.984	3005402.038
13610	36849958	36847768.92	13610	1191.105	3057204.85
13642	36839663	36846659.89	13642	1187.759	3183514.286
13674	36845541	36845550.86	13675	1210.133	3253535.925
13706			13707	1186.361	3193085.179
13739	36885868	36843298.14	13739	1167.409	2802725.098
13769	36839313	36842258.43	13771	1164.65	2828260.021
13804	36841356	36841045.42	13803	1215.918	3011696.331
13835	36846411	36839971.05	13835	1255.524	3185961.491
13867	36840082	36838862.02	13867	1228.425	3111789.482
13899	36839092	36837752.99	13899	1159.993	2737017.155
13931	36838954	36836643.96	13931	1137.067	2630735.778
13963	36827909	36835534.93	13964	1129.367	2761210.77
13995	36826256	36834425.9	13996	1194.851	3163445.332
14027	36828846	36833316.87	14028	1206.953	3548531.618
14059	36824483	36832207.84	14060	1167.15	3583443.007
14092	36810292	36940680.28	14092	1195.994	3527839.027
14122	36697208	36758184.17	14124	1205.368	3692325.143
14155	36553236	36557438.46	14156	1215.314	3697298.435
14188	36391864	36356692.74	14188	1209.836	3618590.521
14220	36202786	36162030.23	14221	1214.732	3576884.098
14252	36013529	35967367.71	14253	1220.326	3518811.312
14284	35815536	35772705.2	14285	1210.064	3357273.384
14316	35613497	35578042.69	14317	1186.932	3254872.458
14349	35422869	35377296.97	14349	1215.743	3259102.008
14380	35222579	35188717.66	14381	1217.015	3266907.442
14412	35010642	34994055.15	14413	1193.401	3117853.46
14445	34806838	34793309.43	14445	1216.819	3100352.859
14477	34604105	34598646.92	14477	1221.925	3157304.339
14509	34397021	34403984.4	14509	1195.294	3063377.964
14541	34184612	34209321.89	14542	1190.615	2955617.706
14574	33997372	34008576.17	14574	1212.942	2933887.587
14605	33804212	33819996.86	14606	1216.609	2935483.246
14637	33616260	33625334.35	14638	1219.182	2941452.803
14669	33416361	33430671.84	14670	1225.164	3073530.24
14701	33198244	33236009.32	14702	1197.809	2936558.818
14736	33086818	33079042.81	14734	1224.118	2847611.148
14768	33084053	33076909.63	14766	1225.32	2862733.757
14798	33071422	33074909.77	14798	1208.368	2769290.755
14831	33078764	33072709.94	14831	1186.588	2589671.875
14862	33068914	33070643.42	14863	1189.632	2650201.493
14894	33062536	33068510.24	14895	1209.852	2762985.742
14927	33060193	33066310.4	14927	1197.57	2791971.896
14959	33066925	33064177.22	14959	1187.95	2787825.208
14991	33063314	33062044.04	14991	1181.145	2717177.541
15023	33051684	33059910.87	15023	1208.505	2826106.119
15055	33055627	33057777.69	15055	1215.827	2912647.265
15087	33052919	33055644.51	15088	1216.561	2868981.104
15119	33049953	33053511.33	15120	1184.684	2791878.107
15152	33052009	33051311.49	15152	1184.195	2704864.352
15183	33043871	33049244.98	15184	1186.329	2751149.683
15216	33046451	33047045.14	15216	1190.788	2866650.387
15248	33050179	33044911.96	15248	1219.051	3005369.257
15280	33045283	33042778.78	15280	1209.301	2912709.871
15312	33042189	33040645.6	15312	1214.132	2891269.103
15344	33036868	33038512.42	15344	1189.6	2827744.15
15376	33030515	33036379.25	15377	1215.456	2826222.785
15409	33046623	33034179.41	15409	1215.219	3453967.369
15440	33038327		15441	1258.181	3915556.445
15473	33034798		15473	1269.194	4264705.374
15505	33024901		15505	1246.914	4459814.757
15537	33026457		15537	1282.827	4626078.511
15569	33029120	33023282.99	15569	1291.004	4976782.763
15601	33022728	33020862.97	15601	1303.436	5138805.684
15633	33018483	33018442.95	15634	1303.568	5142979.046
15665	33013768	33016022.94	15666	1308.087	5211565.934
15697	33013231	33013602.92	15698	1288.456	5136475.031
15730	33010158	33011107.28	15730	1312.903	5137334.934
15762	33009679	33008687.26	15762	1288.966	5164757.573
15794	33008774	33006267.24	15794	1286.454	5064411.207
15826	33003697	33003847.23	15826	1313.211	5218751.452
15858	33001604	33001427.21	15858	1313.932	5272101.07
15890	32997381	32999007.19	15891	1288.334	5152047.778
15922	32992105	32996587.18	15923	1310.035	5160950.728
15955	32990715	32994091.54	15955	1289.915	5223291.361
15987	32991608	32991671.52	15987	1315.872	5154613.486
16018	32983910	32989327.13	16019	1289.836	5186822.928
16051	32986069	32986831.49	16051	1313.738	5179062.033
16083	32978720	32984411.47	16083	1290.309	5202385.87
16115	32978112	32981991.45	16115	1316.579	5239665.785
16147	32984415	32979571.44	16148	1313.265	5249063.151
16179	32981465	32977151.42	16180	1319.146	5208231.162
16212	32983106	32974655.78	16212	1292.293	5033575.968
16242	32912205	32844619.13	16244	1309.691	5010439.788
16273	32726207	32673475.71	16276	1292.529	5002753.328
16308	32526224	32480249.27	16308	1289.841	4939895.547
16340	32326961	32303585.1	16340	1285.179	5012761.749
16372	32121744	32126920.93	16373	1289.247	5006137.075
16404	31916099	31950256.75	16405	1295.74	5061651.269
16437	31722121	31768071.83	16437	1311.104	5172086.167
16469	31540529	31591407.65	16469	1318.251	5233683.256
16501	31369833	31414743.48	16501	1313.682	5040749.541
16533	31194142	31238079.31	16533	1295.02	4873022.872
16565	31014598	31061415.14	16565	1315.057	4816092.987
16597	30849153	30884750.96	16597	1318.785	4808858.228
16629	30683900	30708086.79	16630	1291.658	4668658.992
16661	30511665	30531422.62	16662	1314.557	4531053.192
16694	30355732	30349237.69	16694	1292.153	4450948.974
16725	30197050	30178094.27	16726	1306.161	4453338.497
16757	30032869	30001430.1	16758	1294.034	4517567.546
16789	29851188	29824765.93	16790	1282.742	4370166.906
16822	29678176	29642581	16822	1291.317	4379571.887
16854	29508714	29465916.83	16855	1312.457	4458968.943
16889	29428122	29425464.82	16887	1302.627	4578160.903
16920	29422183	29423524.6	16919	1318.589	4573887.338
16951	29419116	29421584.38	16951	1298.003	4442461.768
16983	29425441	29419581.57	16983	1279.72	4141803.062
17014	29417343	29417641.36	17015	1287.643	4187160.232
17047			17047	1298.983	3985550.74
17079	29430512	29413573.16	17079	1228.218	2839326.269
17110	29403854	29411632.94	17112	1224.648	2888260.753
17144	29406420	29409504.96	17144	1278.667	3567746.626
17175	29405285	29407564.74	17176	1293.71	3872701.749
17207	29399707	29405561.94	17208	1266.35	3834314.999
17240	29396183	29403496.54	17240	1262.864	3856122.748
17272	29398960	29401493.74	17272	1267.706	3974195.074
17304	29403627	29399490.93	17304	1267.589	4011001.125
17336	29400869	29397488.13	17336	1293.721	4165646.688
17368	29391582	29395485.32	17368	1294.747	4270513.095
17400	29391780	29393482.51	17401	1293.343	4294445.471
17432	29390606	29391479.71	17433	1274.459	4276723.186
17465	29391205	29389414.31	17465	1272.348	4271244.47
17496	29383441	29387474.1	17497	1304.704	4395741.56
17529	29382589	29385408.7	17529	1304.157	4522412.548
17561	29385899	29383405.9	17561	1289.824	4778864.709
17593	29384351	29381403.09	17593	1320.216	5110192.672
17625	29385483	29379400.29	17626	1324.866	5765531.441
17657	29376573	29376239.8	17658	1349.168	6105444.095
17690	29376330	29374670.78	17690	1361.396	6470307.809
17721	29376062	29373196.86	17722	1369.54	6801845.712
17753	29371408	29371675.39	17754	1377.145	6923549.017
17786	29367837	29370106.37	17786	1361.789	7038116.947
17818	29370191	29368584.9	17818	1357.781	7101289.234
17850	29365516	29367063.43	17850	1386.263	7229108.405
17882	29363871	29365541.96	17883	1391.564	7401040.836
17914	29365154	29364020.48	17915	1362.834	7291256.865
17946	29367356	29362499.01	17947	1391.929	7455699.481
17978	29361468	29360977.54	17979	1381.36	7537386.967
18011	29354081	29359408.52	18011	1372.427	7542815.273
18043	29356970	29357887.05	18043	1399.975	7674784.491
18075	29359313	29356365.58	18075	1367.367	7605902.26
18107	29349242	29354844.11	18107	1401.907	7742148.629
18140	29351276	29353275.09	18140	1402.044	7833337.765
18171	29351323	29351801.17	18172	1381.614	7766937.085
18203	29353513	29350279.7	18204	1379.428	7791975.665
18235	29343194	29348758.23	18236	1374.145	7813656.568
18268	29345093	29347189.21	18268	1374.812	7893393.425
18300	29346398	29345667.74	18300	1387.121	7985383.881
18332	29349353	29344146.27	18333	1368.178	8017868.961
18364	29347074	29342624.79	18365	1396.456	8100515.784
18396	29342553	29341103.32	18397	1368.175	7748869.813
18429	29338059	29339534.31	18429	1386.321	7619819.358
18461	29335693	29338012.83	18461	1392.34	7755033.942
18493	29335106	29336491.36	18493	1392.107	7750805.751
18525	29332123	29334969.89	18525	1372.373	7718212.832
18557	29331288	29333448.42	18557	1401.089	7845331.565
18589	29338891	29331926.95	18590	1375.181	7822328.425
18620	29289759	29195600.65	18622	1387.207	7923011.596
18651	29149103	29073584.41	18654	1400.822	7847457.816
18685	28980929	28939760.14	18686	1401.57	7821898.52
18718	28820990	28809871.88	18718	1382.286	8012577.155
18750	28675247	28683919.63	18750	1412.973	8481273.672
18782	28519828	28557967.38	18782	1394.15	8477096.296
18814	28371448	28432015.12	18814	1421.626	8391175.758
18847	28240487	28302126.87	18847	1419.959	8397642.712
18878	28117830	28180110.62	18879	1393.531	8290467.993
18911	28012650	28050222.36	18911	1393.051	8282411.599
18942	27883800	27928206.12	18943	1389.684	8346749.871
18975	27761017	27798317.86	18975	1425.306	8590477.768
19007	27648445	27672365.61	19007	1423.159	8524834.516
19039	27532715	27546413.36	19039	1387.26	8114691.612
19071	27417522	27420461.11	19072	1423.505	8513000.382
19103	27299980	27294508.86	19104	1431.811	8873274.165
19135	27186642	27168556.6	19136	1405.413	8687903.151
19167	27069858	27042604.35	19168	1410.665	8575190.132
19200	26959474	26912716.09	19200	1408.319	8529975.254
19232	26858371	26786763.84	19232	1411.622	8386531.953
19266	26812589	26811999.83	19265	1419.998	8330737.857
19297	26816025	26811307.9	19296	1420.903	8250920.854
19328	26811864	26810615.96	19329	1394.114	8140924.85

B

T_{NP} (K)	Oxidation Rate (C/sec/nm^2) - Ramp 1	T_{NP} (K)	Baseline (C/sec/nm^2) - Ramp 1	T_{NP} (K)	Oxidation Rate (C/sec/nm^2) - Ramp 2	T_{NP} (K)	Baseline (C/sec/nm^2) - Ramp 2	T_{NP} (K)	Oxidation Rate (C/sec/nm^2) - Ramp 3	T_{NP} (K)	Baseline (C/sec/nm^2) - Ramp 3	T_{NP} (K)	Oxidation Rate (C/sec/nm^2) -Ending Oxidation
1187.51	0.25494	1197	0.00358	1210	0.11917	1197	0.00102	1202	0.02549	1199	2.07E-04	1198	7.21E-05
1290.22	0.23796	1302	0.00292	1301	0.1166	1293	0.00147	1304	0.01721	1307	9.08E-05		
1386.62	0.19956	1394	0.00403	1407	0.08962	1392	7.93E-04	1396	0.01495	1388	3.07E-04		
1494.19	0.12781	1499	0.00459	1513	0.04803	1514	5.82E-04	1502	0.004	1504	6.47E-05		

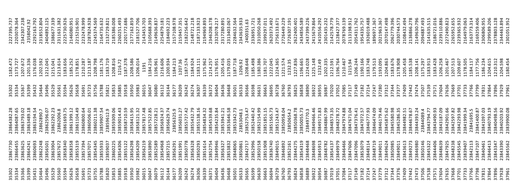

741.74497	747.379	696.012	493.986	469.19	330.31237	307.61016	186.01573	148.18635	223.51642	148.61354
742.02982	728.739	697.847	502.21	470.322	322.07422	308.42116	194.86407	148.76256	167.23842	149.19397
742.31467	747.674	699.685	497.273	471.455	330.44275	309.23348	199.866	149.34041	188.35349	149.77605
742.59949	737.036	701.526	502.915	472.59	325.74117	310.04713	181.07356	149.91991	194.8394	150.35981
742.88431	742.969	703.37	498.581	473.726	328.36332	310.86211	194.33775	150.50105	224.68204	150.94523
743.1691	759.27	705.216	508.358	474.863	335.56773	311.67797	159.57906	151.08383	207.81296	151.53232
743.45389	756.917	707.065	514.095	476.002	334.52779	312.49515	216.91554	151.66827	176.50397	152.12109
743.73866	755.485	708.917	510.145	477.142	333.89491	313.31367	179.52266	152.25436	181.68573	152.71153
744.02342	759.342	710.771	507.144	478.284	335.59955	314.13306	181.96731	152.8421	197.51937	153.30365
744.30816	762.871	712.629	512.167	479.427	337.15923	314.95423	196.8033	153.4315	193.20408	153.89745
744.59289	755.166	714.489	496.557	480.571	333.75392	315.77627	215.86645	154.02256	184.06574	154.49294
744.8776	763.252	716.352	502.931	481.717	337.32762	316.59965	184.32292	154.61528	201.06676	155.09011
745.1623	762.607	718.217	520.739	482.864	337.04255	317.4239	207.12064	155.20966	188.50968	155.68897
745.44698	768.93	720.086	509.08	484.012	339.83707	318.24993	191.58781	155.80571	214.61953	156.28952
745.73165	768.648	721.957	514.068	485.162	339.71244	319.07684	188.96562	156.40343	196.84348	156.89177
746.01631	773.636	723.831	526.64	486.314	341.91694	319.90507	169.33385	157.00283	174.71909	157.49571
746.30095	761.648	725.708	503.612	487.466	336.61871	320.73463	210.88718	157.60389	186.1361	158.10135
746.58558	771.274	727.587	516.645	488.62	340.87303	321.56508	204.14615	158.20663	216.59885	158.7087
746.87019	772.667	729.47	515.751	489.776	341.48868	322.39729	198.14603	158.81106	167.18993	159.31774
747.15479	780.405	731.355	527.907	490.933	344.90857	323.23039	192.47731	159.41716	200.20829	159.9285
747.43938	784.975	733.242	524.408	492.091	346.92834	324.06437	176.43552	160.02495	200.24787	160.54096
747.72395	776.903	735.133	525.86	493.251	343.36083	324.90012	222.50661	160.63442	201.16437	161.15513
748.00851	795.112	737.026	534.2	494.411	351.40849	325.73675	187.72015	161.24558	197.04589	161.77102
748.29305	786.105	738.922	531.698	495.574	347.42775	326.57471	216.18978	161.85843	206.06185	162.38863
748.57758	784.189	740.821	519.876	496.737	346.58095	327.41399	221.10862	162.47298	191.7097	163.00795
748.86209	786.559	742.723	525.863	497.903	347.6284	328.2546	197.15948	163.08923	215.77406	163.629
749.14659	796.652	744.627	536.984	499.069	352.08911	329.09609	185.53454	163.70717	218.66998	164.25177
749.43107	801.603	746.535	528.504	500.237	354.27726	329.93936	207.45586	164.32681	212.93758	164.87626
749.71554	805.403	748.444	542.635	501.406	355.95672	330.78306	198.3255	164.94816	207.74261	165.50249
750	799.43	750.357	532.889	502.577	353.31688	331.62853	203.79313	165.57121	192.82575	166.13045
750.28444	795.61	752.273	533.598	503.748	351.62859	332.47533	218.081	166.19597	220.762	166.76014
750.56887	809.255	754.191	542.047	504.922	357.65915	333.32301	213.73003	166.82244	180.65187	167.39157
750.85328	799.467	756.112	535.206	506.096	353.33323	334.17202	200.02694	167.45062	187.8313	168.02473
751.13768	826.997	758.035	545.086	507.272	365.50042	335.02191	205.08398	168.08052	216.98109	168.65964
751.42207	802.634	759.962	521.553	508.45	354.73293	335.87357	221.50134	168.71214	210.12124	169.2963
751.70644	802.998	761.891	535.344	509.628	354.8938	336.72611	235.59637	169.34547	187.7233	169.9347
751.99079	806.205	763.823	543.154	510.808	356.31117	337.57998	193.37661	169.98053	244.22721	170.57485
752.27513	816.896	765.758	533.171	511.99	361.03617	338.43517	199.91464	170.61732	213.6359	171.21675
752.55946	815.995	767.695	540.657	513.173	360.63797	339.29125	210.02928	171.25583	214.5206	171.8604
752.84377	824.58	769.635	538.31	514.357	364.4322	340.14865	211.64154	171.89607	220.95785	172.50581
753.12807	817.949	771.578	539.314	515.542	361.50156	341.00738	222.87709	172.53805	232.25121	173.15299
753.41235	822.907	773.524	544.627	516.729	363.6928	341.86744	212.85933	173.18176	219.28908	173.80192
753.69662	810.428	775.472	531.676	517.917	358.17757	342.72838	222.59256	173.8272	198.11426	174.45261
753.98088	824.972	777.424	543.046	519.107	364.60545	343.59109	220.0721	174.47439	220.86727	175.10508
754.26512	809.909	779.377	544.936	520.298	357.94819	344.45424	217.62106	175.12331	204.9292	175.75931
754.54934	819.67	781.334	549.114	521.49	362.26217	345.31916	221.98109	175.77398	227.50865	176.41531
754.83356	816.472	783.293	544.134	522.683	360.84878	346.18496	225.19013	176.4264	227.27904	177.07309
755.11775	839.819	785.256	544.339	523.878	371.16725	347.05253	229.70659	177.08057	213.66292	177.73264
755.40193	819.048	787.22	554.825	525.074	361.98727	347.92054	219.74847	177.73648	227.37843	178.39398
755.6861	842.823	789.188	545.944	526.272	372.4949	348.79032	227.37329	178.39416	229.49864	179.05709
755.97026	825.986	791.158	541.202	527.471	365.0536	349.66098	216.83681	179.05358	270.27003	179.72199
756.2544	830.753	793.131	551.689	528.671	367.16043	350.53297	245.77852	179.71477	240.99891	180.38867
756.53852	840.515	795.107	560.966	529.873	371.47485	351.40628	230.56281	180.37771	229.49051	181.05714
756.82263	829.96	797.086	550.8	531.076	366.80995	352.28093	221.00297	181.04242	232.00301	181.72741
757.10673	836.938	799.067	558.131	532.28	369.89396	353.15645	237.55451	181.7089	227.33442	182.39946
[illegible]	[illegible]	[illegible]	[illegible]	[illegible]	[illegible]	[illegible]	[illegible]	[illegible]	[illegible]	[illegible]

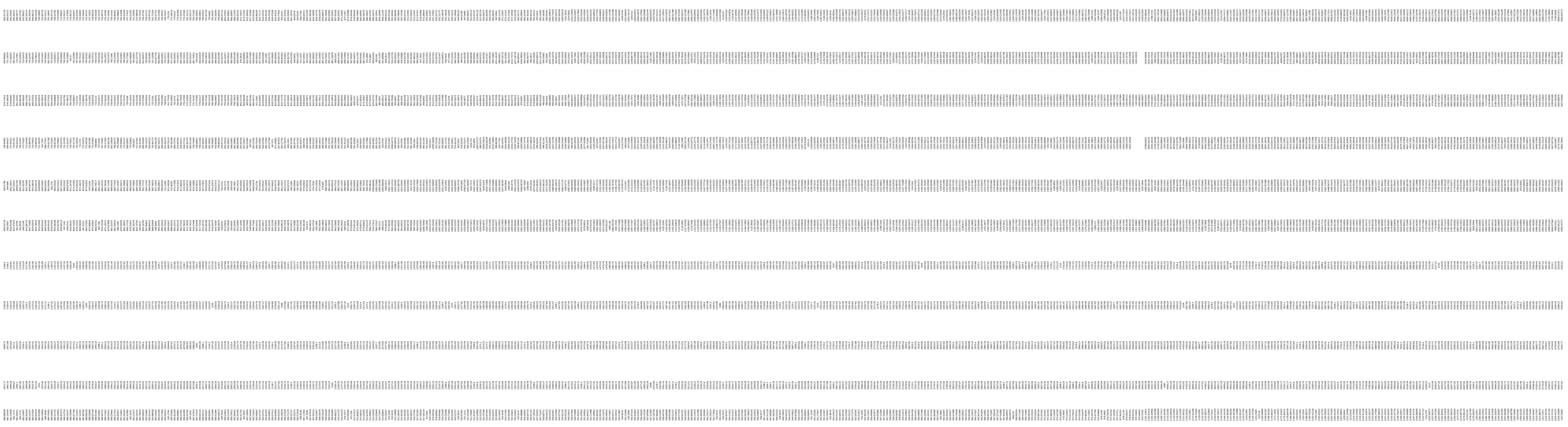

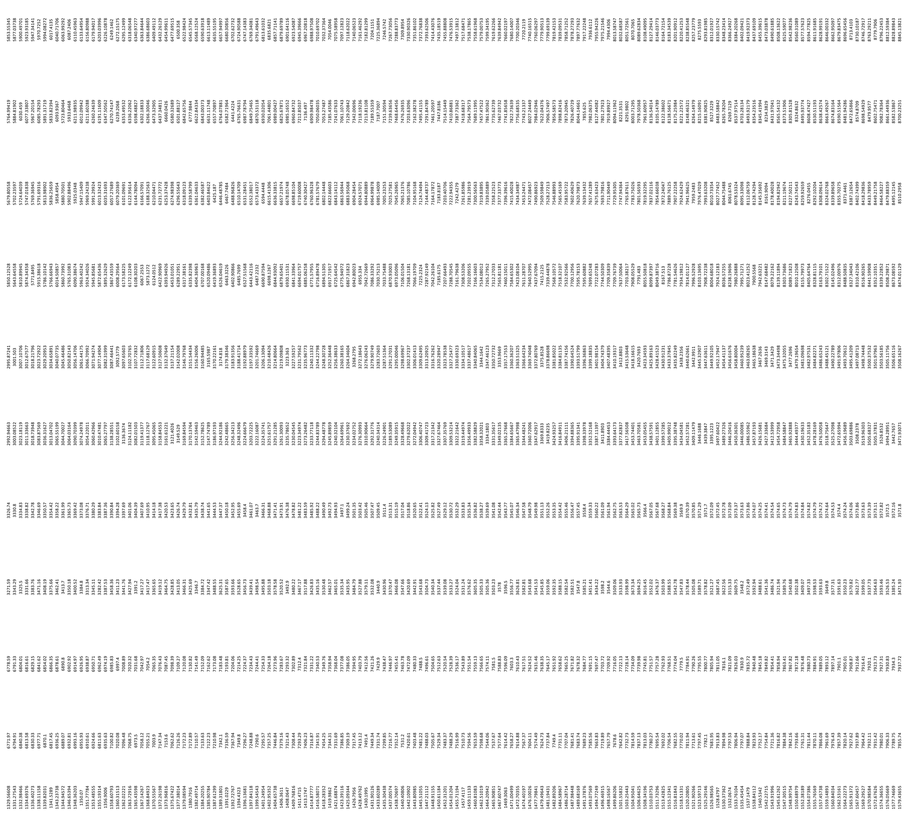

Time (s)	Mass (Da)	Mass (Da) - Reg	O_2 (Torr)	Time (s)	T_{NP} (K)	I_{NP} (Photons/sec/sr)	Laser Power (mW)
11130	26513262	26520431.5		11002	1694.152	15628555.44	40.91542
11163	26513202	26514787.7		11034	1707.374	15708900.49	41.14191
11194	26508828	26509485.95		11066	1705.96	15881531.64	40.89237
11226	26502639	26504013.17		11098	1685.501	15793778.79	40.70809
11259	26493662	26498369.37		11130	1708.931	15877294.58	41.11876
11291	26486364	26492896.59		11163	1713.946	15898873	40.84084
11323	26495073	26487423.81		11195	1704.059	15744612.86	40.42735
11355	26491907	26481951.03		11227	1706.737	15509713.02	40.39003
11387	26469587	26476478.25		11259	1713.363	15605734.74	40.11314
11420	26465299	26470834.45		11291	1702.335	15333921.31	39.68434
11452	26470661	26465361.67		11323	1689.795	15059223.67	39.73611
11483	26459182	26460059.92		11355	1702.662	15017032.93	40.1866
11516	26457347	26454416.11		11387	1700.962	15297762.7	40.18155
11547	26448375	26449114.36		11420	1716.04	15331967.48	40.09654
11580	26447772	26443470.56		11452	1718.071	15559256.74	39.59528
11612	26443787	26437997.78		11484	1702.88	15030105.79	39.16858
11644	26435613	26432525		11516	1687.573	14722425.52	39.21925
11676	26425543	26427052.23		11548	1713.109	14838342.55	39.57542
11709	26428389	26421408.42		11580	1712.982	15090695.85	39.07284
11740	26408752	26416106.67		11612	1695.032	14793592.15	38.66437
11773	26421629	26410462.87		11644	1691.554	14474830.7	38.68937
11804	26414983	26405161.12		11677	1686.258	14447442.74	38.9875
11837	26416671	26399517.31		11709	1696.417	14606145.44	39.42696
11868	26398578	26394215.56		11741	1713.124	15039858.23	39.32834
11901	26386275	26388571.76		11773	1685.098	14827533.79	39.00565
11932	26342005	26383270	2.12E-05	11805	1692.103	14595145.94	39.47966
11961	26140889	26027787.56	2.12E-05	11837	1708.533	14930170.15	39.59175
11996	25891097	25588704.69	2.13E-05	11869	1699.265	15020406.83	39.4161
12026	25489501	25212347.74	2.12E-05	11901	1704.642	14993439.28	39.41132
12055	25001396	24848535.79	2.13E-05	11933	1693.38	14852254.25	39.44685
12084	24411856	24484723.95	2.13E-05	11966	1703.417	14835163.25	39.68125
12119	23942232	24045640.58	2.13E-05	11998	1702.15	14894072.56	39.68958
12149	23441542	23669283.51	2.13E-05	12030	1679.52	14341215.97	39.77205
12180	22906741	23280381.33	2.12E-05	12062	1679.878	14198906.53	40.30253
12219	22595548	22791117.27	2.13E-05	12094	1700.039	14741264.04	40.7251
12250	22278535	22402214.47	2.13E-05	12126	1716.039	15085560.44	40.5956
12278	21845701	22050948.24	2.13E-05	12158	1721.272	14606714.36	40.08629
12309	21411079	21662046.07	2.13E-05	12190	1698.464	13780744.8	39.68923
12343	21017323	21235507.8	2.13E-05	12223	1688.506	13256778.83	39.7711
12382	20832009	20746243.74	2.13E-05	12255	1679.931	13070695.59	40.27639
12417	20722816	20307160.37	2.31E-04	12287	1681.835	12871258.93	40.78218
12440	20442998	20018620.08	1.35E-05	12319	1672.479	12625310.88	41.40266
12476	20205976			12351	1673.143	12592246.35	42.64269
12517	20203800	20202771.18		12383	1681.341	13040180.97	43.76729
12543	20200115	20201655.59		12415	1708.099	13585458.76	44.07738
12576	20200427	20200239.65		12447	1713.78	13689445.39	43.7736
12608	20201086	20198866.61		12479	1695.944	13113767.41	43.41647
12639	20196187	20197536.48		12512	1692.323	12875511.18	43.44673
12672	20193300	20196120.54		12544	1683.157	12935647.21	43.75186
12704	20193135	20194747.5		12576	1704.227	13037657.38	44.12884
12736	20194054	20193374.47		12608	1715.272	13337094.45	44.01007
12768	20191883	20192001.43		12640	1696.471	13164321.42	43.66053
12800	20191937	20190628.4		12672	1693.259	13034152.54	43.74435
12832	20187303	20189255.36		12704	1710.191	12981125.33	43.77211
12865	20189184	20187839.42		12736	1699.796	13250459.13	43.41978
12896	20187690	20186509.29		12769	1698.785	12893531.3	43.42708
				12801	1712.916	12987810.8	43.28495
				12833	1697.493	12931618.47	42.91591
				12865	1691.367	12699753.28	42.96224
				12897	1702.739	12759971.7	43.12812

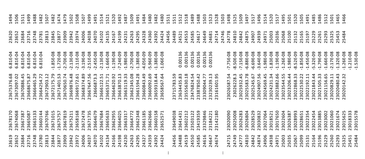

	T_{NP} (K)	C/O_2 Collision
Fig. 1	1187.51	0.00165
	1290.215	0.00154
	1386.617	0.00129
	1494.188	8.29E-04
Fig. 2	1399.056	1.24E-04
	1498.949	1.38E-04
	1598.755	1.47E-04
	1698.25	1.15E-04
	1797.956	6.73E-05
	1899.497	7.42E-05
	1997.446	2.44E-05
	2098.339	2.72E-05
	2198.227	3.01E-05
	2298.08	-1.25E-04
Fig. 3	1599.549	1.65E-04
	1700.472	4.84E-05
	1798.661	7.72E-05
	1897.782	1.76E-05
	2000.723	1.46E-06
	2095.877	3.89E-06
Fig. 4A	1600	8.59E-04
	1600	0.00175
	1600	5.18E-05
Fig. 4B	1200	0.00115
	1200	0.00115
	1200	3.89E-06
Fig. 6	1700	0.00307
Fig. 7	1899.043	2.55E-04
	1899.043	7.75E-04
	1899.043	4.48E-05
Fig. 8	1501.149	2.05E-04
	1501.149	3.33E-04
	1501.149	6.88E-05
Fig. S3	1201.069	2.32E-04
	1294.148	2.67E-04
	1397.481	2.83E-04
	1527.768	3.21E-04
	1597.348	2.20E-04
	1692.114	1.48E-04
Fig. S4	1212	2.17E-04
	1299.618	3.06E-04
	1393.763	2.76E-04
	1498.129	3.01E-04
	1602.641	1.97E-04
	1704.483	1.42E-04
	1796.891	1.27E-04
	1873.159	1.32E-04
Fig. S6	1700.547	4.24E-05
	1797.55	3.59E-05
	1897.959	2.59E-05
	1994.867	3.45E-05
	2089.131	3.55E-05
Fig. S7	1700	1.37E-04
	1700	1.37E-04
	1700	6.64E-06
Fig. S8	1500	6.28E-04
Fig. S9	1890.648	4.25E-04
	1890.648	5.23E-04
	1890.648	2.60E-04